

# Microwave Control of the Tin-Vacancy Spin Qubit in Diamond with a Superconducting Waveguide

Ioannis Karapatzakis<sup>1,\*</sup>, Jeremias Resch<sup>1,\*</sup>, Marcel Schrodin<sup>1</sup>, Philipp Fuchs<sup>2</sup>, Michael Kieschnick<sup>3</sup>,  
 Julia Heupel<sup>4</sup>, Luis Kussi<sup>1</sup>, Christoph Sürgers<sup>1</sup>, Cyril Popov<sup>4</sup>, Jan Meijer<sup>3</sup>,  
 Christoph Becher<sup>2</sup>, Wolfgang Wernsdorfer<sup>1,5</sup> and David Hunger<sup>1,5,†</sup>

<sup>1</sup>*Physikalisches Institut (PHI), Karlsruhe Institute of Technology (KIT),  
 Wolfgang-Gaede-Straße 1, 76131 Karlsruhe, Germany*

<sup>2</sup>*Department of Physics, Saarland University, Campus E2 6, 66123 Saarbrücken, Germany*

<sup>3</sup>*Division of Applied Quantum Systems, Felix-Bloch-Institute for Solid State Physics, University of Leipzig,  
 04103 Leipzig, Germany*

<sup>4</sup>*Institute of Nanostructure Technologies and Analytics (INA),  
 Center for Interdisciplinary Nanostructure Science and Technology (CINSaT),  
 University of Kassel, Heinrich-Plett-Straße 40, 34132 Kassel, Germany*

<sup>5</sup>*Institute for Quantum Materials and Technologies (IQMT), Karlsruhe Institute of Technology (KIT),  
 Herrmann-von-Helmholtz Platz 1, 76344 Eggenstein-Leopoldshafen, Germany*

 (Received 7 March 2024; revised 11 June 2024; accepted 18 July 2024; published 27 August 2024)

Group-IV color centers in diamond are promising candidates for quantum networks due to their dominant zero-phonon line and symmetry-protected optical transitions that connect to coherent spin levels. The negatively charged tin-vacancy (SnV) center possesses long electron spin lifetimes due to its large spin-orbit splitting. However, the magnetic dipole transitions required for microwave spin control are suppressed, and strain is necessary to enable these transitions. Recent work has shown spin control of strained emitters using microwave lines that suffer from Ohmic losses, restricting coherence through heating. We utilize a superconducting coplanar waveguide to measure SnV centers subjected to strain, observing substantial improvement. A detailed analysis of the SnV center electron spin Hamiltonian based on the angle-dependent splitting of the ground and excited states is performed. We demonstrate coherent spin manipulation and obtain a Hahn echo coherence time of up to  $T_2 = 430 \mu\text{s}$ . With dynamical decoupling, we can prolong coherence to  $T_2 = 10 \text{ ms}$ , about a sixfold improvement compared to earlier works. We also observe a nearby coupling  $^{13}\text{C}$  spin, which may serve as a quantum memory, thus substantiating the potential of SnV centers in diamond and demonstrates the benefit of superconducting microwave structures.

DOI: [10.1103/PhysRevX.14.031036](https://doi.org/10.1103/PhysRevX.14.031036)

Subject Areas: Atomic and Molecular Physics,  
 Quantum Physics, Quantum Information

## I. INTRODUCTION

Optically addressable coherent spins in the solid state are favorable candidates for the realization of quantum networks [1,2]. Among them, color centers in diamond have enabled demonstrations of the full set of functionalities in this context, including spin-photon [3,4] and spin-spin entanglement [5,6], teleportation [7], and the first demonstrations of a three-node network [8]. Group-IV color centers

in diamond have recently emerged as a promising system, in particular, due to their excellent optical properties: Their inversion symmetry leads to a dominant zero-phonon line and reduced sensitivity against electrical noise, which has enabled, e.g., the incorporation of silicon-vacancy centers in optical nanocavities [9,10] and the demonstration of quantum network elements [6,9,11]. However, the presence of two orbital ground states opens a decoherence channel for the spin levels via phonon scattering. In this respect, the tin-vacancy (SnV) center offers advantages due to its large ground-state splitting of more than 800 GHz, such that phonons at this frequency can be frozen out at comparably high temperatures greater than 1 K. Reported dephasing times for all-optical control range from 1.3  $\mu\text{s}$  [12] to 5  $\mu\text{s}$  at a temperature of 2 K [13], with coherence times ranging from 0.3 ms using all-optical control [12] to 1.6 ms for microwave control [14], respectively. However, direct spin control by

\*These authors contributed equally to this work.

†Contact author: david.hunger@kit.edu

*Published by the American Physical Society under the terms of the Creative Commons Attribution 4.0 International license. Further distribution of this work must maintain attribution to the author(s) and the published article's title, journal citation, and DOI.*

microwave fields is hampered by orthogonal orbital contributions to the Zeeman states. Recently, it has been shown that by introducing strain, orbital mixing can be induced and high-fidelity microwave control becomes possible [14,15]. This regime makes the level structure nontrivial and motivates an accurate mapping of the spin Hamiltonian, which is, however, still partially missing and treated inconsistently in the literature. In particular, the quenched Zeeman splitting of the quantized orbital momentum has not been precisely determined yet [14–16].

In this paper, we characterize the negatively charged SnV center regarding its magneto-optical properties and determine the relevant components, such as the orbital quenching factors from a full fit of the electronic spin Hamiltonian. We explain the properties of the ground and excited states under strain and the relevant qubit transitions, as well as the influence of an external magnetic field. We demonstrate coherent control of the electron spin and reach a  $T_2$  time of 10 ms by using standard dynamical decoupling sequences. A simplified design and fabrication process demonstrates the potential of the SnV center for quantum computing, communication, and the establishment of robust quantum networks.

## II. ELECTRONIC STRUCTURE OF STRAINED SNV CENTERS

It has been observed that microwave control of group-IV defects is only achievable under a strained environment of the emitters [14,15,17–19], explained by the orthogonality of the electron orbital states of the two spin qubit levels. However, recent work suggests that efficient microwave spin control is possible for specific combinations of the microwave  $B_{ac}$  and magnetic field  $B_{dc}$  orientations even in the absence of strain [20]. Still,  $B_{ac}$  is predefined by the design of the microwave antenna, and thus the main handle is the orientation of the  $B_{dc}$  field with respect to the defect's symmetry axis. The role of strain is to enhance the overall microwave response of the SnV electron spin by mixing the orthogonal orbitals and thus relaxing the magnetic dipole selection rules, allowing microwave control for almost all magnetic field orientations. Therefore, we intentionally induce strain in our sample. In our experiment, we use a square diamond membrane with a width of 1 mm cut along the  $\langle 110 \rangle$  directions and a (001) surface. The diamond membrane has a thickness of 26  $\mu\text{m}$ , with the top and bottom layers removed by reactive ion etching to eliminate surface damage caused by polishing [21]. SnV centers are generated by implantation of 65-keV tin ions into the membrane, a subsequent annealing to 1200  $^\circ\text{C}$ , and boiling in a tri-acid mixture [22]. The membrane is glued on a silicon substrate using a UV-curing adhesive (NOA63, Norland products). Utilizing an adhesive with a significantly different coefficient of thermal expansion compared to that of diamond serves as a simple procedure to intentionally induce strain within the diamond membrane.

Although the silicon substrate has a more than twofold larger thermal expansion coefficient than diamond, its contribution to the induced strain is negligible according to our simulation results; see Appendix E.

Our experiments are performed in a home-built dilution refrigerator reaching temperatures as low as 50 mK. The sample is mounted on a cold finger and accessed through windows in the thermal shields of the cryostat. Optical addressing of the SnV center is achieved through a confocal microscope setup, as described in Appendix A 2.

In Fig. 1(a), the energy-level scheme of a strained SnV center is illustrated. Spin-orbit interaction splits the zero-phonon line (ZPL) into the  $E_{g,u}^{1/2}$  and  $E_{g,u}^{3/2}$  doublets, where the  $\frac{1}{2}$  and  $\frac{3}{2}$  superscripts refer to the total angular momentum while  $g$  and  $u$  refer to the ground and excited states, respectively [16]. In photoluminescence (PL) measurements, the effect of strain is observable as an increased splitting between the two doublets in the ground and excited states. The resulting splitting is depicted by blue and red arrows for the C and D transitions, respectively. The Zeeman interaction lifts the degeneracy of the doublets and allows for individual addressing of the states by resonant optical excitation or microwave driving. The optically allowed (forbidden) transitions are indicated as black (gray) arrows. The spin qubit is shown as orange-colored energy levels. In Fig. 1(d), the PL measurements of an unstrained (SnV-D) and a strained (SnV-B) SnV center are shown. To quantify the strain effect of the adhesive to the SnV centers, we measure the PL spectra of over 400 emitters along the diamond membrane and select the spectra with precisely distinguishable pairs of C and D transitions as depicted in Fig. 1(e). With growing distance to the diamond edge, the component  $\epsilon_{A_1}$  of the strain tensor, which corresponds to a shift of the ZPL [17], increases. This result is directly observed in the spectra of the SnV centers, where the ZPL at the center of the membrane shifts up by 1 nm compared to the unstrained case. On the other hand, the ground-state splitting, dominated by the  $\epsilon_{E_{xy}}$  components [17], remains nearly constant with an average value of 1.32(0.48) THz, as depicted in the lower part of the figure. This result is observed for equally prepared samples, although the absolute value of the strain can vary for individual samples, depending, e.g., on the thickness of the adhesive. The combination of the strain components qualitatively explains the behavior of the strain-tuned emitters and is consistent with a COMSOL simulation; see Appendix E.

## III. MAGNETO-OPTICAL PROPERTIES OF THE SNV CENTER

### A. Hamiltonian of the SnV center

As a first step, we aim for a comprehensive characterization of the SnV center's optical and magnetic properties. The Hamiltonian for group-IV defects is originally derived from measurements on silicon-vacancy centers [23].

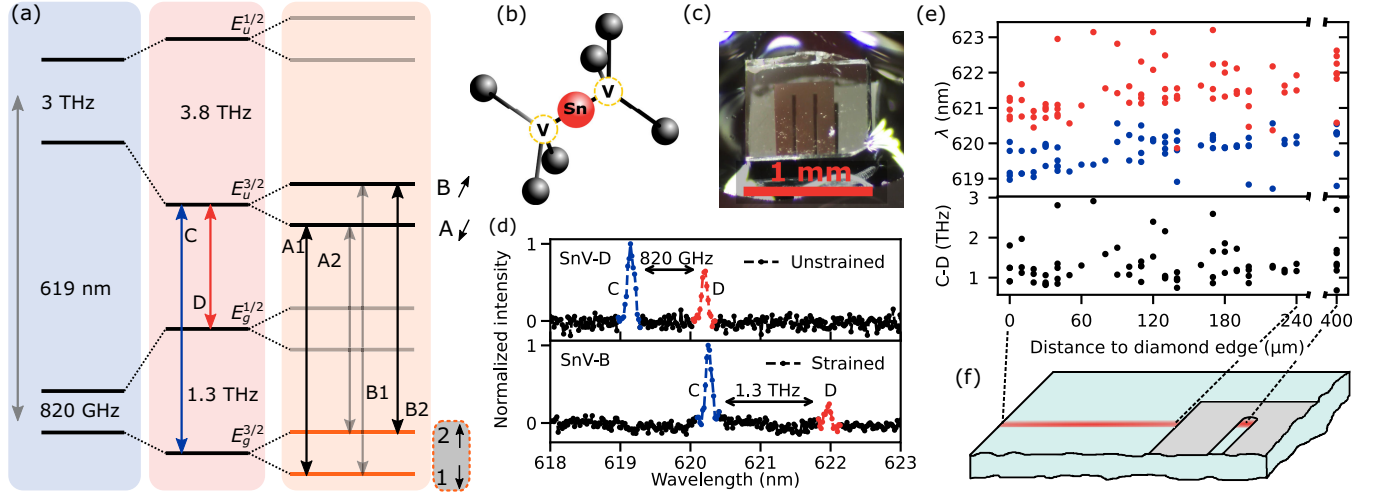


FIG. 1. Strained SnV center in a diamond membrane with a coplanar waveguide. (a) Energy-level scheme of a strained SnV center in a magnetic field. The C and D transitions are depicted as blue and red arrows, respectively. A magnetic field further splits the spin states, and the black (gray) arrows indicate the allowed (forbidden) transitions. The qubit is indicated by orange-colored energy levels. (b) Schematic of the SnV center in diamond showing the interstitial Sn-atom neighbored by two vacancies inside the diamond lattice. (c) Optical image of the sample fixed onto a silicon substrate with an adhesive. The niobium coplanar waveguide is fabricated on top of the diamond for microwave control. (d) Photoluminescence spectra of an unstrained (SnV-D) and a strained (SnV-B) SnV center with the C (D) transition marked in blue (red). The measurements are performed at 4 K showing only the ground-state splitting. (e) Top: strain-induced shift of the C and D transitions of SnV centers measured along the membrane from the edge of the diamond to the center. Bottom: corresponding ground-state splitting C-D in terms of frequency. The PL measurements are taken within the area marked in red on the diamond membrane schematic in diagram (f), with the superconducting CPW depicted in gray.

Here, we use a Hamiltonian that directly relates to each of the four spin-orbit doublets  $E_{g,u}^{1/2}$  and  $E_{g,u}^{3/2}$ , resulting in an effective Hamiltonian given by

$$\hat{H}_{\text{eff}}^{g,u} = -\lambda^{g,u} \hat{L}_z \hat{S}_z + \mu_B (f_{m_j}^{g,u})_{\{\pm\frac{1}{2}, \pm\frac{3}{2}\}} \cdot \hat{L}_z B_z + g_s \mu_B \hat{S} \cdot \mathbf{B} + \hat{Y}_{\text{strain}}. \quad (1)$$

The first term accounts for the effective spin-orbit splitting with the strength of the spin-orbit coupling  $\lambda^{g,u}$  for the orbital ground and excited states. Note that  $\hat{L}_z$  and  $\hat{S}_z$  are the  $z$  components of the angular momentum operator and the Pauli-matrix vector  $\hat{S} = \frac{1}{2}(\hat{\sigma}_x, \hat{\sigma}_y, \hat{\sigma}_z)^T$ . The second term corresponds to the orbital Zeeman effect that contains the Bohr magneton  $\mu_B$  and the quenching factor  $f_{m_j}^{g,u}$  that corrects the orbital Landé  $g$  factor, i.e., describes the smaller splitting opposed to the expected splitting for a quantized magnetic moment. This quenching factor can be separated into two parts:  $f_{m_j}^{g,u} = p_{m_j}^{g,u} \cdot g_l^{g,u}$ , where  $p_{m_j}^{g,u}$  is the contribution from the dynamic Jahn-Teller effect (DJT), known as the Ham effect, and  $g_l^{g,u}$  is the Steven's orbital quenching factor, arising from lowered symmetry of the system [16]. Each magnetic quantum number  $m_j = \pm\frac{1}{2}$  and  $m_j = \pm\frac{3}{2}$  corresponds to one of the electronic states of the spin-orbit doublets split by the applied external magnetic field  $\hat{B}$ . Attributing a separate quenching factor to each single orbital with corresponding  $m_j$ , instead of using an

averaged quenching with an asymmetry [14–16], allows for a precise determination of the orbital quenching in the presence of different strain environments. For instance, for an unstrained emitter, the qubit frequency that corresponds to the splitting of the  $E_g^{3/2}$  doublet is purely determined by the  $m_j = \pm\frac{3}{2}$  orbitals. Hence, an average quenching factor  $f^g$  for the two ground-state doublets cannot be extracted, as it lacks a meaningful physical basis. However, the  $m_j = \frac{1}{2}$  substrates contribute for strained emitters, as we show in the derivation of the Hamiltonian in Appendix B, and can be extracted as a consequence. We use four separate sets of data, each from different emitters, with unstrained (SnV-D), low-strain (SnV-A), and high-strain (SnV-B and SnV-C) properties, and follow a step-by-step approach in our fitting routine to determine the quenching factors for all ground- and excited-state doublets. The third term in the effective Hamiltonian in Eq. (1) is the electron Zeeman contribution with the electron  $g$  factor ( $g_s = 2$ ). Finally, the fourth term gives the strain contribution  $\hat{Y}_{\text{strain}}$ , which contains the diagonalized strain contributions  $\alpha$ , for the ground and excited states, respectively. For an in-detail discussion and matrix form representations, we refer to Appendix B.

## B. Analysis of magnetic field-dependent transitions

In the following, we discuss the influence of strain on the electronic spin's optical addressability and fit the Hamiltonian to our measurements. In Figs. 2(a) and 2(b)

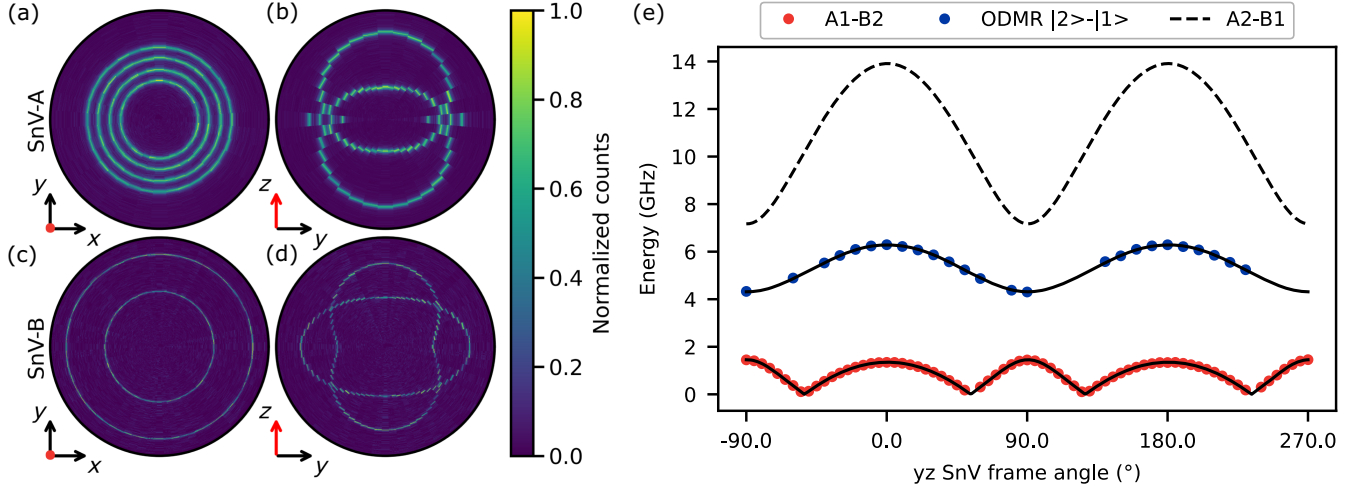


FIG. 2. Optical properties of the strained SnV center under different magnetic field orientations at 8 K. The magnetic field is rotated within the respective frame of the SnV center, where the  $z$  axis aligns with the symmetry axis, indicated in red, of the SnV center. (a),(b) Splitting of the allowed A1 and B2 and forbidden A2 and B1 transitions of the low-strain SnV-A with  $\Upsilon^g = 35.0(15)$  GHz measured by PLE scans shown in polar coordinates, where the radial axis spans a 2.3-GHz range, as well as measured with  $25 \text{ MHz s}^{-1}$  scanning speed under varying  $B$ -field orientations with 190-mT amplitude. (c),(d) Splitting of the A1 and B2 transitions of the high-strain SnV-B with  $\Upsilon^g = 577.3(34)$  GHz measured by PLE scans within a 4.3-GHz range and  $50 \text{ MHz s}^{-1}$  scanning speed under varying  $B$ -field orientations with 190-mT amplitude. (e) Fit of the electronic energies of SnV-B to the observed optical spin conserving transitions A1 and B2 in the SnV frame (red points). The qubit transition frequencies (blue points) are measured in ODMR scans at 50 mK. The spin-forbidden transitions A2 and B1 are not measured due to their large splitting.

[Figs. 2(c) and 2(d)], the dependence of the optical transitions on the magnetic field orientation of the low (high) strain SnV-A (SnV-B) is presented. The image shows photoluminescence excitation (PLE) measurements of the spin-conserving optical transitions A1 and B2 at a temperature of 8 K. The magnetic field orientation is given in polar coordinates within the respective frame of the SnV center. The  $z$  axis aligns with the symmetry axis, indicated in red, of the SnV center. The radial axis corresponds to the frequency of the PLE scans at fixed polar coordinates. These data are obtained by preceding measurements of the A1 and B2 transitions in the lab frame under an external magnetic field rotation. With the SnV quantization axis obtained in this way, we acquire  $xy$  and  $yz$  rotation maps; i.e., the external magnetic field is rotated in both polar  $\theta$  and azimuthal  $\phi$  directions in the frame of the investigated emitter. During the measurement, the magnetic field magnitude is held constant at  $B_{\text{dc}} = 190$  mT. The radial axis in Fig. 2 spans over 2.3 GHz and 4.3 GHz of the excitation laser frequency for SnV-A and SnV-B, respectively. We note that the absolute magnitude of the external magnetic field plays a crucial role for the precision of the determined quenching factors. Thus, we include a thorough uncertainty analysis of the calibration process of the magnetic field strength in Appendix B. Scanning in the  $xy$  plane as seen Figs. 2(a) and 2(c), i.e., perpendicular to the quantization axis, serves to validate the experimental precision and to gain insight into the strain magnitude of the orbital ground and excited states. In the presence of strain, the degeneracy of these transitions is lifted. This

result can be directly observed by the separation of the optical lines. Furthermore, for SnV-A in Fig. 2(a), along with the two allowed transitions A1 and B2, the two forbidden transitions A2 and B1 can be seen, as a result of spin mixing under these conditions. The energy separation of the A1 and B2 transitions measured for magnetic field rotations in the  $yz$  plane allows a further constraint on the Hamiltonian. Figure 2(e) perfectly shows this difference for SnV-B as a function of the polar angle in the  $yz$  plane using red points. Additionally, the qubit transitions are determined from optically detected magnetic resonance (ODMR) measurements and depicted as blue points. The data can be fully described by the Hamiltonian given in Eq. (1).

In our procedure, we first determine the ground-state splitting of an unstrained emitter (SnV-D) through PL measurements, as illustrated in Fig. 1(d). The absence of strain is validated by the preserved degeneracy of the A1 and B2 transitions under a perpendicular magnetic field; see Appendix B 2 and Fig. 14. We determine the spin-orbit interaction for the ground state to be  $\lambda^g = 822(1)$  GHz, matching previous reports for high-temperature treated samples [24]. For all strained SnV centers, like the two depicted in Fig. 2, the ground-state strain  $\Upsilon^g$  is related to the ground-state splitting by the relation  $\Delta_g = \sqrt{(\lambda^g)^2 + 4(\Upsilon^g)^2}$ .

We use the determined spin-orbit coupling  $\lambda^g$  as input to find the ground-state strain magnitude by matching it to the minimum of the qubit transitions  $\nu_{\text{qubit}}(\theta)$  at  $\theta = 90^\circ$ , as this frequency solely depends on  $\Upsilon^g$  for a given magnetic field strength. For the excited-state strain  $\Upsilon^u$ , we fit the

Hamiltonian at the same angle  $\theta = 90^\circ$  to the measured allowed transition splitting, assuming a spin-orbit coupling for the excited state of  $\lambda^u = 3000$  GHz [16,25].

In the next step, we determine  $f_{\frac{3}{2}}^g$  by fitting the qubit transitions of a low-strain emitter (SnV-A) with  $\Upsilon^g = 35(15)$  GHz. This value is completely independent from all other quenching factors, when fitted to the qubit transitions. By fixing this value, we can now determine  $f_{\frac{3}{2}}^u$ , fitting to the allowed transition splitting of SnV-A. The  $f_{\frac{1}{2}}^{g,u}$  values cannot be determined in the case of low strain, as their influence is negligible due to the absence of orbital mixing. However, in the case of moderate and high strain where  $\lambda \ll \alpha$  does not apply, the influence of the quenching factors with  $m_j = \pm \frac{1}{2}$  increases. Hence, we use the obtained values for  $f_{\frac{3}{2}}^{g,u}$  from SnV-A to further determine the  $f_{\frac{1}{2}}^g$  value by fitting to the qubit transitions of the highly strained SnV-B. Here, the  $f_{\frac{1}{2}}^g$  sublevel of the ground state significantly contributes to the energy levels of the qubit in the diagonalized Hamiltonian. It is, however, insensitive to  $f_{\frac{1}{2}}^u$  from the excited state. Lastly, we determine the remaining value by fitting to the allowed transitions of SnV-B. To validate our fitting procedure, we use the data set obtained by an additional emitter (SnV-C) and compare the measurement data with the fitting parameters; see Figs. 11(e) and 11(f). The final fitting parameters and the corresponding errors are shown in Table I. We note that the precise Hamiltonian parameters are necessary to understand spin polarization, readout, and the angle dependence of the optically allowed transitions, as well as the qubit frequency. In addition, the provided parameters are of major assistance when working with uncharacterized SnV centers, for instance, when the optically allowed transitions A1 and B2 are no longer visible due to optical spin initialization at temperatures below 4 K.

## IV. COHERENT CONTROL

### A. Superconducting coplanar waveguide

With the collected understanding of the spin Hamiltonian, we redirect our attention to the coherent manipulation of the electron spin. In recent studies on microwave spin control of SnV center qubits in diamond [12,14,15], drive-induced heating has been identified as a significant limitation. It plays a pivotal role in limiting the spin lifetime  $T_1$  and increasing the infidelity of quantum operations.

We briefly examine these limitations arising from intrinsic Ohmic losses by fabricating a normal conducting microwave coplanar waveguide made of gold on a diamond sample. We study an SnV center approximately 10  $\mu\text{m}$  away from the central conductor and measure the photon counts under resonant excitation. After initialization in the off-resonant spin state, the emitter remains dark at low temperature, given the long spin relaxation time. We then

TABLE I. Parameters of the SnV center Hamiltonian. The spin-orbit splitting  $\lambda^g$  is measured by PL measurements from an unstrained SnV center (SnV-D). For the magnetic field magnitude values, we estimate an error of 0.5%. The strain components and orbital quenching factors are obtained by a fit to the electron spin Hamiltonian.

Parameter	Value	Fitted	Source
$\gamma_l$	14 GHz T <sup>-1</sup>	...	[26]
$\gamma_s$	28 GHz T <sup>-1</sup>	...	[27]
$\lambda^g$	822(1) GHz	Yes	SnV-D
$\lambda^u$	3000 GHz	...	[16,25]
$f_{\frac{3}{2}}^g$	0.268(13)	Yes	SnV-A
$f_{\frac{1}{2}}^g$	0.251(12)	Yes	SnV-A
$f_{\frac{3}{2}}^u$	0.486(15)	Yes	SnV-B
$f_{\frac{1}{2}}^u$	0.500(8)	Yes	SnV-B

	SnV-A	SnV-B	SnV-C
$\Upsilon^g$	35.0(15) GHz	577.3(34) GHz	530.0(40) GHz
$\Upsilon^u$	60.0(70) GHz	961.90(49) GHz	921.4(32) GHz
$B_{\parallel}$	193.44(97) GHz	193.46(97) mT	193.47(97) mT
$B_{\perp}$	193.48(97) mT	189.03(95) mT	193.45(97) mT
$\delta\theta$	-0.08(2) $^\circ$	-0.54(2) $^\circ$	-0.46(18) $^\circ$

apply an off-resonant microwave pulse of 10 ms length and observe that, already at moderate microwave input powers around 0 dBm, the photon count instantly increases and follows a nontrivial behavior for different microwave powers. We interpret the increasing count rate as a reduced  $T_1$  time originating from an instant heating effect upon the application of microwaves, followed by diffusion of the locally induced heat into the cryostat. The precise local temperature is impossible to determine with conventional thermometers, as the heat dissipates over the large distance from the SnV center towards the thermometer. However, heat is instantly felt by the SnV center, and it is detectable by observing the count rate under resonant excitation of one spin state. From our measurements, we can deduce that the temperature-dependent lifetime  $T_1$  is reduced by several orders of magnitude and the count rate increases by thermal repopulation of the continuously pumped readout state. While this effect can be interesting for temperature sensing at temperatures below 4 K, it poses a bottleneck for microwave control. For more details and the measurement data, we refer to Appendix A 4.

In order to overcome this obstacle arising from microwave-line heating, we make use of the absence of Ohmic losses of superconducting metals [28] and fabricate a coplanar waveguide (CPW) made from niobium. Niobium, with a high critical temperature of around 9.2 K [29], is a suitable material for microwave control even at elevated temperatures that are commonly achieved in bath or cryogen-free cryostats. To evaluate the CPW for our microwave control measurements, we first determine the properties of superconducting

waveguides (SC-CPW). On a bulk diamond substrate, a continuous CPW is fabricated via all-optical lithography, as is shown in the inset in Fig. 3(a). The CPW has a thickness of 50 nm and is fabricated by electron-beam evaporation. In Fig. 3(a), we depict the measured insertion loss (S21) of the coaxial lines and the waveguide at a frequency of 3 GHz as a function of the temperature that is acquired during the cooldown of the cryostat. With decreasing temperature, the total resistance decreases continuously, apart from a sharp drop at around 9 K, when the niobium film enters the superconducting state. The residual losses arise from impedance mismatch and the normal-conducting coaxial lines inside the cryostat. The electric current through the waveguide is proportional to the effective  $B_{ac}$  and to the square root of the applied microwave power. For that reason, we evaluate the superconductor in terms of the maximum applicable power. The microwave power is measured directly in front of the cryostat for all measurements. Figure 3(b) shows the transition from the superconducting to the normal-conducting state at a power of 19 dBm. No magnetic field was applied for these measurements.

For the microwave spin control measurements, we use a simple SC-CPW design with a short circuit at the waveguide's end; see Fig. 1(c). We simulate the waveguide in the presence of the dielectric environment and analytically determine the required size of the CPW gaps. This analysis

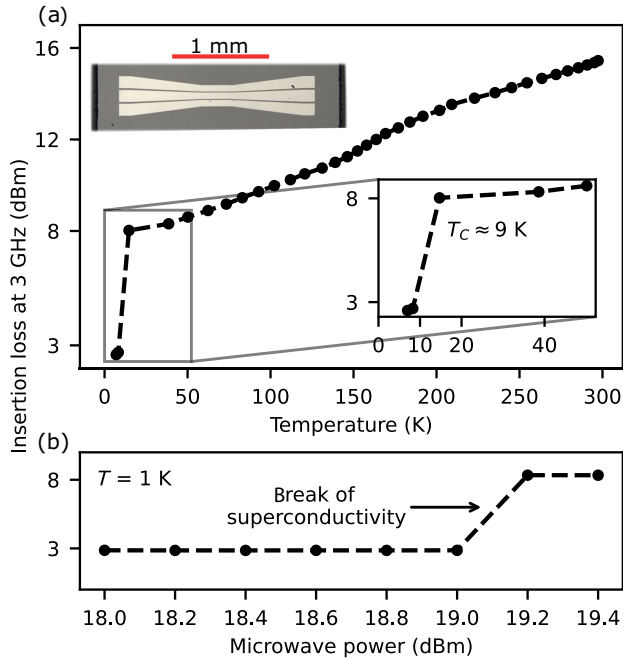


FIG. 3. Properties of superconducting niobium waveguides. (a) Insertion loss (S21) of a superconducting CPW at a frequency of 3 GHz. The enhanced transmission at less than or close to 9 K is caused by the superconducting phase transition and the vanishing resistance. The CPW for the reference measurements is depicted in the inset in panel (a) and was fabricated on a bulk diamond. (b) Breaking of superconductivity at a power of 19 dBm.

ensures that the characteristic impedance matches the impedance of  $Z_0 = 50 \Omega$  of the transmission lines into the cryostat, avoiding reflections through impedance mismatch. By taking the dielectric properties of the silicon substrate, the polymer, and the diamond membrane into account [30], we determine the size of the gaps between the conductors to 24  $\mu\text{m}$  for conductors with a width of 150  $\mu\text{m}$ .

## B. Microwave spin control

In the next step, we make use of the SC-CPW for coherent spin control. By applying an external magnetic field, the lower  $E_g^{3/2}$  doublet splits into the spin states  $|1\rangle$  and  $|2\rangle$ , which can be used as a qubit. Here, we demonstrate coherent control of the SnV under a parallel magnetic field of  $B_{\parallel} = 96$  mT at a temperature of 50 mK. The initialization of the electron spin is achieved by resonantly driving one of the allowed optical transitions, either A1 or B2, as seen in Fig. 1(a). We achieve an initialization fidelity of up to  $F = 99.0 \pm 0.1\%$ , which is limited by the dark counts of the single photon detector, as shown Fig. 4(a). The optical cyclicity is particularly high for the parallel field orientation, yielding a high readout signal but also increasing the initialization time. The latter can be adjusted by modifying the excitation power of the resonant laser beam. We observe a highly stable negative charge state of the SnV center and thus do not implement an off-resonant repump pulse in our control sequences. If occasionally necessary, the charge is regained by a 532-nm repump pulse with excitation power below 100 nW to avoid spectral diffusion due to changes in the charge environment [25]. We determine our qubit frequency via ODMR measurements as shown in Fig. 4(b) by using continuous microwave chirps. The microwave frequency is swept within a fixed time of 10 to 20 ms under continuous resonant optical driving using power on the order of 1 nW and repeated until the desired signal-to-noise ratio is achieved. To achieve high spectral resolution, we use low microwave amplitudes at insertion powers as low as  $-40$  dBm (100 nW) into the cryostat. We observe two resonances for parallel magnetic field orientation at 3144.34(22) MHz and 3148.58(26) MHz, with a linewidth of 838.65(82) kHz. The separation indicates strong coupling to a proximal spin. From the beating in the spin-echo measurements (see Appendix B 1 Fig. 10), we infer that the splitting originates from a single  $^{13}\text{C}$  nuclear spin. Such coupled nuclear spins can serve as a long-lived quantum memory [31,32].

Figure 4(c) illustrates a Rabi measurement at a 14-dBm insertion power, showing a Rabi frequency of  $\Omega/2\pi = 4.31(28)$  MHz that corresponds to a  $\pi$  pulse of 115 ns. The full contrast and absence of decay illustrate the high fidelity [ $F = 99.1(+0.3)(-2.3)\%$ ] of the spin manipulation. In the chevron pattern of the Rabi oscillation, the coupling to the nuclear spin is directly visible by the presence of two resonances where the Rabi frequency is minimal. However, the measured pattern is not reproduced by the sum of two

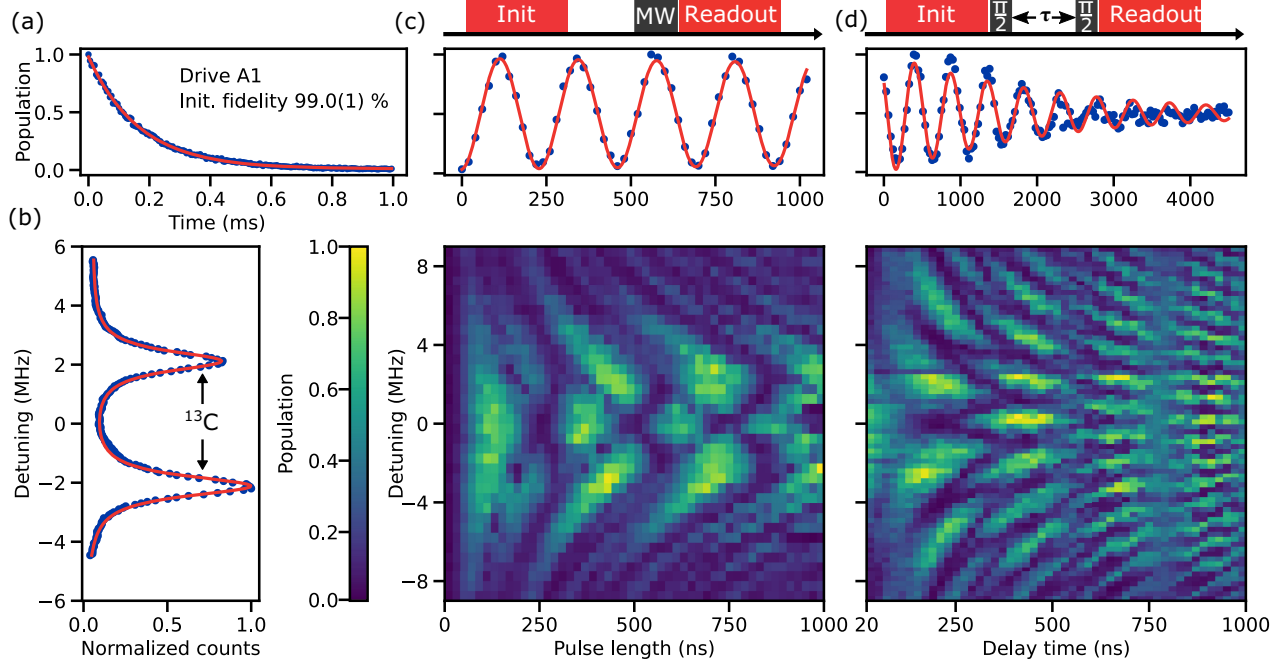


FIG. 4. Coherent manipulation of the electron spin at 50 mK. (a) Selective spin initialization of A1 with an initialization fidelity of 99.0(1)%. (b) ODMR with continuous wave excitation. Two resonances are observed due to coupling to a proximal nuclear spin. The red line corresponds to a double Lorentzian fit with center frequencies 3144.34(22) MHz and 3148.58(26) MHz and a linewidth of 838.65 (82) kHz. (c) Exemplary Rabi oscillation. Top: scheme for resonant initialization, coherent driving, and resonant readout. Single oscillation with a Rabi frequency of  $\Omega/2\pi = 4.31(28)$  MHz at 14 dBm. Bottom: 2D chevron pattern with varying detuning showing a beating due to the hyperfine structure. Both plots share the same  $x$  axis. (d) Ramsey measurement at the center frequency. Data points can be fitted by a sinusoidal wave with an exponential decay of 2.1(2)  $\mu$ s. Bottom: 2D Ramsey pattern. Both plots share the same  $x$  axis.

independent detuned Rabi oscillations as one may expect for a thermal nuclear spin. The deviation can be explained by electron-nuclear correlations that are introduced by driving the electron spin under conditions where the hyperfine coupling to the nuclear spin is of the same order of magnitude as the qubit's Rabi frequency [33]. This mechanism can be used for coherent nuclear spin control [31].

Performing free-induction decay measurements allows us to probe the dephasing time of the system. From the envelope of a Ramsey measurement tuned to the center between the two resonances, as pictured in Fig. 4(d), we determine a dephasing time  $T_2^* = 2.1(2)$   $\mu$ s of the qubit, which is of the same order as for isotopically pure overgrown diamond [14]. As we detune the driving frequency relative to the two transitions, the signal oscillates and forms a crownlike pattern, with instances of a full loss of coherence again stemming from the coupling to the proximal nuclear spin.

### C. Dynamical decoupling

The coherence time  $T_2$  can be increased significantly compared to  $T_2^*$  by making use of echo techniques. First, we measure the coherence time for a Hahn echo measurement. We resonantly drive to one nuclear spin resonance with a microwave power of 10 dBm, resulting in a Rabi

frequency of 2.5 MHz. We determine a coherence time  $T_2 = 179 \pm 4$   $\mu$ s [ $T_2 = 433(23)$   $\mu$ s] for the parallel (perpendicular) field orientation; see Fig. 5(a). The higher coherence time for a perpendicular field orientation can be attributed to the decoupling from the electron spin bath [15]. To further extend the coherence time, we incorporate the Carr-Purcell-Meiboom-Gill (CPMG) sequence, which consists of multiple refocusing  $\pi$  pulses, shifted in phase with respect to the first  $\pi/2$  pulse. As a perpendicular magnetic field orientation results in a very small cyclicity of the readout state and thus requires many repetitions to achieve reasonable SNRs, we measure all CPMG sequences with a parallel field orientation. Figure 5 shows the measurements for up to 64 refocusing pulses, increasing the coherence time to  $T_{2,\text{CPMG64}} = 10(1)$  ms, which is about sixfold improved compared to earlier work [14]. The fidelity of the decoupling decreases for a higher number of pulses, as more and more pulse errors due to the coupling of the proximal nuclear spin are added. However, we determine the scaling of  $T_2$  with the pulse number and find an almost linear scaling  $T_2 \propto N^\beta$ , with  $\beta = 0.95(9)$ . This finding is in contrast to the expected scaling for a single nuclear spin bath [34,35] of  $\beta = 2/3$ . We attribute this difference to the presence of a second electronic spin bath in addition to the nuclear spin bath [15,19,36,37]. By describing the total bath with a double-Lorentzian power spectral density with

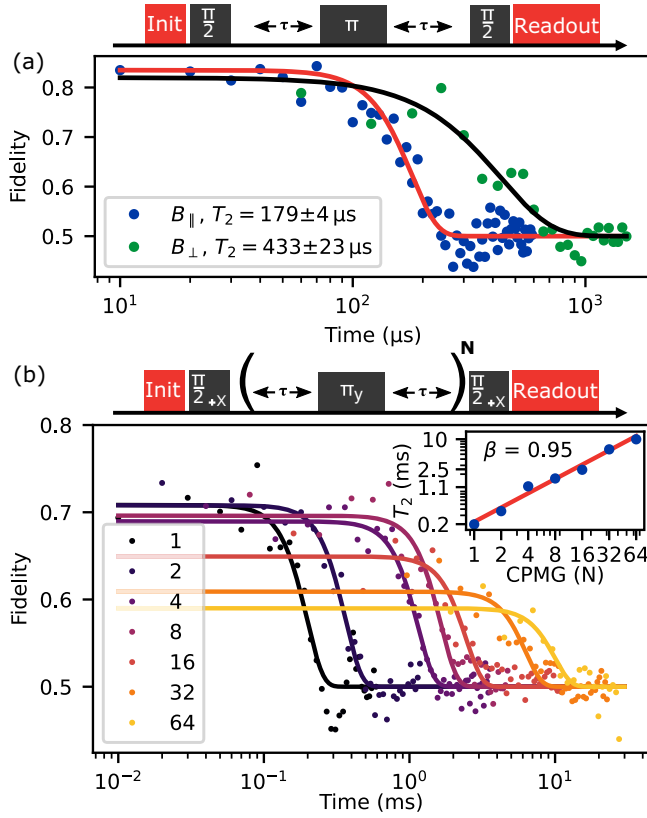


FIG. 5. Coherence measurements. (a) Hahn echo measurements under a parallel and perpendicular applied magnetic field. (b) CPMG sequence with varying number  $N$  refocusing pulses. The data are fit to stretched exponential envelopes with  $e^{-(t/T_2)^{\xi}}$ , where  $\xi = 4$ . The inset shows a double-logarithmic plot of a power-law behavior  $T_2 \propto N^{\beta}$ , with  $\beta = 0.95$ .

a sharp frequency cutoff for the electronic spin bath [19,38], the observed scaling close to  $\beta = 0.95$ , as well as the stretching exponential  $\xi = 4$ , can be reproduced. For further discussion, we refer to Appendix C.

## V. CONCLUSION

In this work, we demonstrate extended control over the optical and magnetic levels of the SnV center electron spin, thereby contributing to a deeper understanding of these properties. We show a simple procedure to incorporate strain into the diamond to allow for microwave control. We measure 2D rotation maps of the optical transitions under varying magnetic field orientations to determine the SnV axis with less than  $1^\circ$  uncertainty. We develop a fitting procedure for the optical and microwave transitions to the Hamiltonian of the electron spin, using the explicit doublets for each total angular momentum, which allows for a qualitative determination of the orbital quenching factors. We use niobium to avoid drive-induced heating. We measure long coherence times of up to  $T_2 = 10(1)$  ms in a CPMG sequence. The almost linear scaling of the

coherence time with the number of pulses shows potential for further improvement. For higher fidelity of the signal, pulse errors can be minimized by using optimized control pulses [39,40], shorter  $\pi$  pulses, and initialization of the proximal nuclear spin [33]. We observe detuning-corrected Rabi frequencies of 3.6 MHz (5.3 MHz) for parallel (perpendicular) orientation of the magnetic field for a driving power of 14 dBm. Rabi drive can be further enhanced by optimizing the design of the CPW. The existing layout incorporates wide gaps to effectively address a large number of emitters. Narrower gap sizes and tapered lines enable higher Rabi frequencies [19]. We have shown that the use of superconducting waveguides allows for efficient control of the SnV center electron spin, achieving long coherence times. Our careful analysis of the electron spin Hamiltonian provides valuable insights for further investigations of the response of the SnV center under coherent driving [20]. The observed coupling to a proximal  $^{13}\text{C}$  nuclear spin promises future possibilities to manipulate and store quantum information in its long-lived spin state.

## ACKNOWLEDGMENTS

We thank Tim Schröder, Gregor Pieplow, Mohamed Belhassen, and Dennis Rieger for helpful discussions, Eckhard Wörner from Diamond Materials for cutting and notching the sample, and Jonathan Körber for support in the early stage of the experiment. This work was partly supported by the German Federal Ministry of Education and Research (Bundesministerium für Bildung und Forschung, BMBF) within the projects “QR.X” (Contracts No. 16KISQ004, No. 16KISQ001K, and No. 16KISQ005) and “SPINNING” (Contract No. 13N16211), the Deutsche Forschungsgemeinschaft (DFG) through CRC TRR 288–422213477 “ElastoQMat” (Project A08) and TRR 306–429529648 “QuCoLiMa,” the Kompetenzzentrum Quantencomputing Baden-Württemberg (Contract No. QC-4-BW), and the Karlsruhe School of Optics and Photonics (KSOP).

## APPENDIX A: EXPERIMENTAL DETAILS

### 1. Sample fabrication

The sample used in these experiments is an electronic grade diamond membrane from Element Six with dimensions  $2 \times 2 \times 0.04$  mm and an initial surface roughness of 4 nm (2.3 nm) on side A (side B). Both sides are strain-relief etched by reactive ion etching. To remove damage from polishing, the parameters we use for the etching procedure are as follows:

- (i) Side A: 50 min Ar/ $\text{Cl}_2$  + 5  $\times$  (7 min Ar/ $\text{Cl}_2$  + 13 min  $\text{O}_2$ ),
- (ii) Side B: 20 min Ar/ $\text{Cl}_2$  + 5  $\times$  (7 min Ar/ $\text{Cl}_2$  + 15 min  $\text{O}_2$ ) + 10 min Ar/ $\text{Cl}_2$  + 15 min  $\text{O}_2$ .

For further information, see similar works, e.g., Ref. [21]. In total, a thickness of 7  $\mu\text{m}$  is removed on each side,

leading to a surface roughness of 3 nm (side A) and 2 nm (side B).

As side B has a lower surface roughness, it is used for implantation of tin ions. The isotope  $^{116}\text{Sn}$  is implanted with a fluence of  $1 \times 10^9 \text{ cm}^{-2}$  and an energy of 65 keV. The sample is annealed post-implantation for 4 h at 1200 °C at a pressure of less than  $1 \times 10^{-6}$  mbar. To clean the surface, the sample is boiled in a tri-acid mixture (1 : 1 : 1, nitric acid:sulfuric acid:perchloric acid) at 400 °C. Afterwards, the sample is laser cut into four pieces by Diamond Materials. Finally, the membrane is baked on a hotplate for 6 h at 450 °C and cleaned in boiling piranha acid. All measurements are performed on SnV centers within the two pieces, SnV-2-B1 and SnV-2-B2, depicted in Fig. 9(a). The sample SnV-2-B2 on the left hosts SnVs B, C, and D. We note that SnV-D has been measured in the center region of the sample before the waveguide fabrication and without induced strain. The sample SnV-2-B1 hosts SnV-A. In Table II, we provide a summary of the different characterized SnV centers with a brief description of the respective measurement figures.

For the CPW fabrication, we glue one piece of the diamond on a  $4 \times 4$  mm silicon wafer with a UV-curing adhesive. We use the AZ5214E photoresist in our all-optical lithography process and deposit a 50-nm-thick niobium layer by electron-beam evaporation. For the lift-off procedure, we use acetone and undertake a final cleaning step with water.

## 2. Setup

The data in this work are measured in a home-built dilution cryostat with a base temperature of 50 mK. The sample is mounted on a copper cold finger that is thermalized to the mK plate with silver strands. The cold finger is mounted on piezoelectric steppers (2 ANPx101/RES/LT, ANPz101/RES/LT, ANC300-controller, Attocube). Optical excitation and readout are performed in a home-built confocal setup (see Fig. 6).

Resonant laser pulses are generated by a tunable continuous-wave laser source (C-WAVE vis, Hübner), locked to a wavemeter (WS7, HighFinesse), in addition to an acousto-optical modulator (3200-1214, G&H). The trigger signals are generated using a fast Transistor-transistor (TTL) logic (ADwin-Pro II, Jäger). The microwave signal is generated by an arbitrary waveform generator (AWG70001A, Tektronix). Charge repump of the SnV center is applied by a continuous-wave 532-nm laser (Ventus MPC6000, Laser Quantum) and triggered by TTL logic (Adwin Gold II, Jäger). A magnetic field of up to 1.5 T is created by a home-built, superconducting, 3D vector magnet around the microscope objective (MPLN100X, Olympus). The excitation laser is scanned using a galvo mirror system (GVS212, GPS011-power supply, Thorlabs). Fluorescence is separated by a 90:10 beam splitter (BSN10, Thorlabs) and additional filters (BLP01-532R-25, FF01-593/LP-25, LP01-633R-25, Semrock). Finally, the signal is focused through a pinhole onto an avalanche photodetector (SPCM-AQRH-16, Excelitas). PL spectra are taken with a fiber-coupled spectrometer (SP-2500i, Princeton Instruments). The characterization measurements on the superconducting waveguide are performed with a Keysight VNA E5071C.

## 3. Microwave power characterization

We use coaxial transmission lines for microwave delivery within the cryostat, extending up to the mK stage. For the sample, we use a custom-made CPW fabricated on a flexible printed circuit board, featuring 18  $\mu\text{m}$  thick copper conductors and a 100  $\mu\text{m}$  thick polyimide dielectric.

The insertion loss (S21) through the cryostat, including the flexible CPW cable, is shown in Fig. 7(a). The total loss at 3 GHz amounts to approximately 4 dB. Because of the symmetry of the setup, we expect half the total losses at the sample position. The dips in transmission at approximately 4.3 and 8.6 GHz are caused by radiation losses arising from standing waves between the evenly spaced vias with 1-mm

TABLE II. Overview of the four SnV centers, A–D, and the respective measurement figures.

SnV	Sample	CPW	ZPL (THz)	Strain	Fig. 1	Fig. 2	Fig. 4	Fig. 5
A	SnV-2-B1	Au	484.134	Low	...	(a),(b) 2D PLE	...	...
B	SnV-2-B2	Nb	483.269	High	(d) PL	(c),(d) 2D PLE, (e) $\hat{H}$ fit	Coherent control	(a) Echo, (b) CPMG
C	SnV-2-B2	Nb	483.388	High	...	...	...	...
D	SnV-2-B2	...	484.131	Unstrained	(d) PL	...	...	...

SnV	Fig. 8	Fig. 10	Fig. 11	Fig. 12	Fig. 13	Fig. 14	Fig. 15	Fig. 17
A	(c) Heating	...	(a),(b) $\hat{H}$ fit	$f$ error	...	...	...	...
B	(a) ODMR, (b) $T_1$	$^{13}\text{C}$ bath	(c),(d) $\hat{H}$ fit	$f$ error	Lifetime, FWHM ZPL	...	CPMG	Chevron $B_{\perp}$
C	...	...	(e),(f) Verify $\hat{H}$	...	...	...	...	...
D	(b) $T_1$	...	...	...	...	2D PLE	...	...

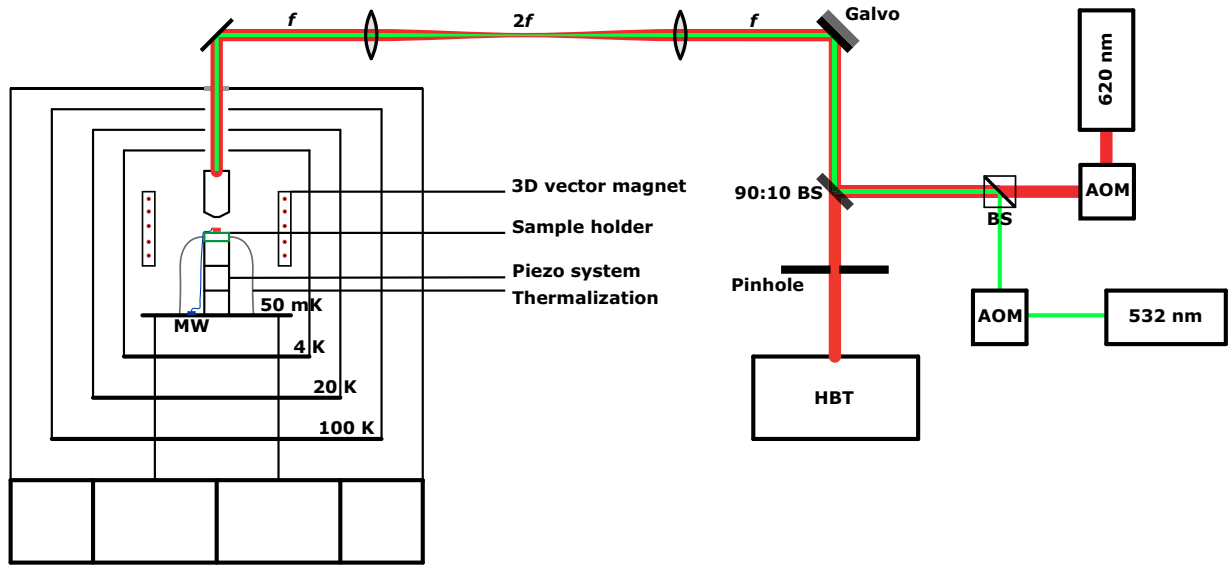


FIG. 6. Schematic of the experimental setup. Optical addressing and readout of the SnV centers is performed by a home-built confocal setup, depicted by the red (green) beam paths for resonant (off-resonant) excitation. Sideband fluorescence is separated by a 90:10 beam splitter and long-pass filters (not depicted) and focused through a pinhole onto avalanche photodiodes arranged in a Hanbury Brown-Twiss setup. The sample is mounted on a piezo stack inside a home-built dilution cryostat with a base temperature of 50 mK. Scanning over the sample is achieved by two galvo mirrors arranged in a  $4f$  setup, where the objective is mounted onto the 4 K stage. Magnetic fields are applied using a superconducting 3D vector magnet around the focal point of the objective.

distance ( $\lambda/4$  radiation). The vias connect the CPW ground planes on the top side with the ground plane on the backside of the flexible cable. The fast oscillations are due to standing waves within the ends of the cable, probably due to imperfect soldering of the SMA connectors to the flexible part. Since we only use one half of the cable, as depicted in Fig. 7, the influence of the vias is significantly reduced and the oscillations are eliminated.

The measurements regarding the properties of the niobium waveguide in Fig. 3 are performed with the Keysight VNA E5071C. Here, the excitation scheme for

all VNA measurements is a nonaveraged linear and discrete frequency sweep with 10,000 data points and a duration of approximately one second per measurement. For the cooldown measurements in Fig. 3(a), the sweep range is 0.1–14 GHz, and the output power is fixed at  $-10$  dBm. For the power measurements in panel (b), the sweep range is 2–4 GHz. For both measurements, the data points corresponding to 3 GHz were extracted. No magnetic field was applied for these measurements.

For coherent control, we use a microwave power of 14 dBm for the 2D Rabi and Ramsey measurements and

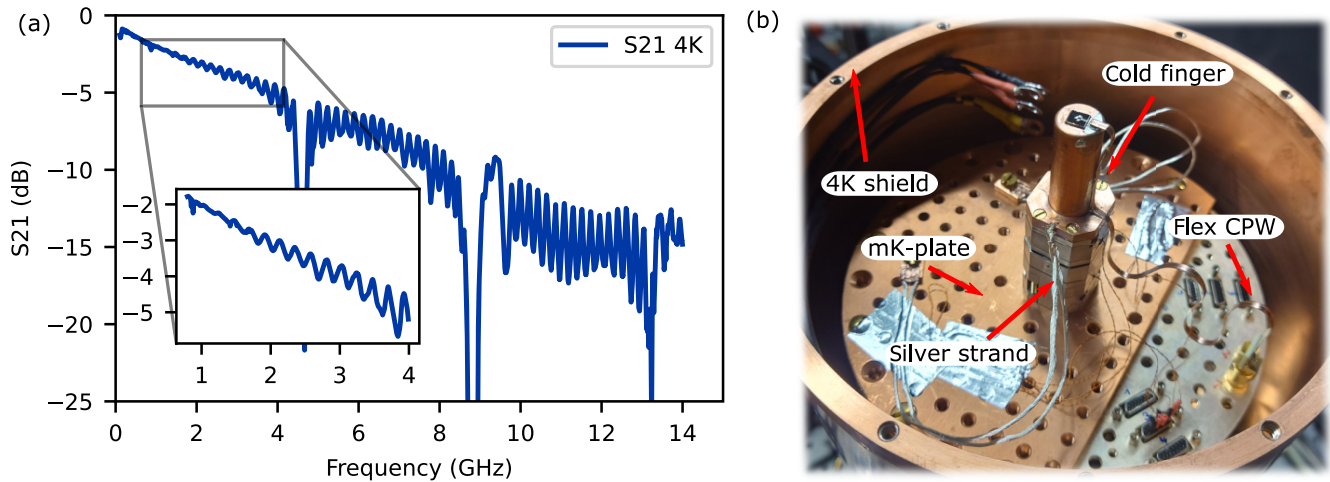


FIG. 7. Insertion loss through the cryostat and mK plate. (a)  $S_{21}$  at 4 K from the coaxial input of the cryostat to the output including the flexible CPW cable. (b) mK plate of the cryostat. Microwaves reach the sample on the cold finger via bonding wires from the flexible CPW to the SC-CPW on the sample.

10 dBm for the CPMG measurements. The power for all measurements is directly measured in front of the cryostat. In this context, the power corresponds to the instantaneous power derived from the microwave amplitude. The averaged power is determined over the duty cycle of the measurement. Typically, for a Hahn echo measurement with a  $\pi$  pulse of 115 ns and perpendicular field orientation, the duty cycle is approximately 1:100 due to the low cyclicity of the optical transition, resulting in a fast electron spin initialization rate. Conversely, for parallel field orientation, where the initialization time is much longer, the duty cycle is approximately 1:10000. The initialization for parallel field orientation is illustrated in Fig. 4(a).

In Fig. 7(b), the mK plate of the cryostat is depicted. Microwave delivery occurs via the custom-made flexible CPW, which is connected to the SC-CPW on the sample using aluminum bonding wires.

#### 4. Heating effects of NC-CPW vs SC-CPW

To qualitatively understand the heating effects of normal-conducting (NC) versus superconducting (SC) coplanar waveguide antennas, we use the SnV center as a temperature sensor to roughly estimate the local temperature of the sample during microwave application. We note that the measurements on NC-CPW are performed on SnV-A, which exhibits low strain, while the SC-CPW measurements are performed on the high-strain SnV-B, which is used for the coherent control measurements in the main text.

For SnV-A, we use a magnetic field of 193 mT with an angle of  $\theta = 60^\circ$  to split the optically allowed transitions as well as the qubit transitions. At this angle, the low-strain SnV still exhibits high cyclicity and thus a high readout signal, but simultaneously, the spin initialization time is reduced to the order of  $\mu\text{s}$  for excitation powers in the low-nW range. Starting at a base temperature of 50 mK, we apply an off-resonant microwave pulse with a length of 10 ms and a frequency of 3 GHz to quantify the heating effect. We continuously initialize the SnV into the dark spin state by exciting the A1 transition. After the microwave pulse, we wait for 190 ms to allow the heat to diffuse into the cryostat. We repeat this sequence until the signal-to-noise ratio is satisfactory. We observe an increasing count rate during the microwave pulse, as is shown in Fig. 8(c). Interestingly, for high microwave powers above 10 dBm, the count rate rises continuously even after the microwave is switched off. To roughly estimate the local temperature of the SnV center, we compare  $T_1$  measurements previously performed on the unstrained SnV-D. At temperatures below 4 K, the lifetime  $T_1$  of the spin is already above one millisecond, as is shown in Fig. 8(b). At the base temperature of the cryostat, the spin lifetime is  $T_1 > 1$  s. The increased count rate during the heating of the microwave line indicates that the local temperature of the SnV center rises above 4 K, causing the pumped state to be continuously thermally repopulated.

We attempt the same measurement for the high-strain SnV-B with the SC-CPW; however, no increase in count rate could be observed, even for microwave powers that break the superconductivity. We attribute this result to the noticeably higher spin lifetime of SnV-B due to the larger ground-state splitting. Figure 8(b) illustrates the difference of the spin lifetimes for the unstrained and highly strained SnV centers, where SnV-B already shows a spin lifetime of 2.59(45) ms at 6.43(3) K.

As an alternative, we perform ODMR measurements at high microwave powers to understand the superconducting nature of the CPW. At a magnetic field of 93 mT applied parallel to the quantization axis of SnV-B, we apply a microwave chirp for 10 ms followed by a 190-ms waiting time, similar to the measurement procedure described above. The resulting measurements are depicted in Fig. 8(a). We observe almost no change up to 14-dBM microwave power; notice, however, the drastically decreasing signal for higher powers. The count rate does not increase during or after the microwave pulse, even after transitioning to the normal-conducting state. Thus, we assume the temperature of the SnV center remains below 6K. We note that the superconductivity breaks with less microwave power than in Fig. 3 in the main text, due to the applied magnetic field of  $B_{\text{dc}} = 93$  mT.

A measurement of the critical field of the SC-CPW, is shown in Fig. 9(b). The critical field  $B_{c2}$  is reached at around 0.95 T for a temperature of 6.5 K and is already 1 order of magnitude larger than the field strength used in the coherent control measurements in the main text. Additionally, the critical magnetic field of niobium at an operating temperature of 50 mK is above the maximum field strength achievable with the coils, which, in the pure  $z$  direction, is 1.33 T. Thus, we have not been able to measure the critical field at such low temperatures. We remark that further investigation is necessary to qualitatively characterize the ac losses of the superconducting waveguide, especially in combination with an applied magnetic field and higher frequencies. The samples with NC-CPW and SC-CPW are depicted in Fig. 9(a).

## APPENDIX B: ELECTRON SPIN HAMILTONIAN

### 1. Calibration of the dc magnetic field

We initially estimate the magnetic field via COMSOL simulations, which typically exhibit low error. However, since the quenching factors are very sensitive to errors in the magnetic field strength, we further refine our measurements using the SnV as a sensor. To determine the magnetic field strength as precisely as possible, we measure the response of the  $^{13}\text{C}$  nuclear spin bath in both the parallel and perpendicular orientations to the SnV axis. This approach allows us to calculate the absolute current dependence of our magnetic field coils for all subsequent measurements. With a Larmor precession of  $\gamma_{^{13}\text{C}} = 10.7084$  MHz T $^{-1}$  of the nuclear spin, the strength of the

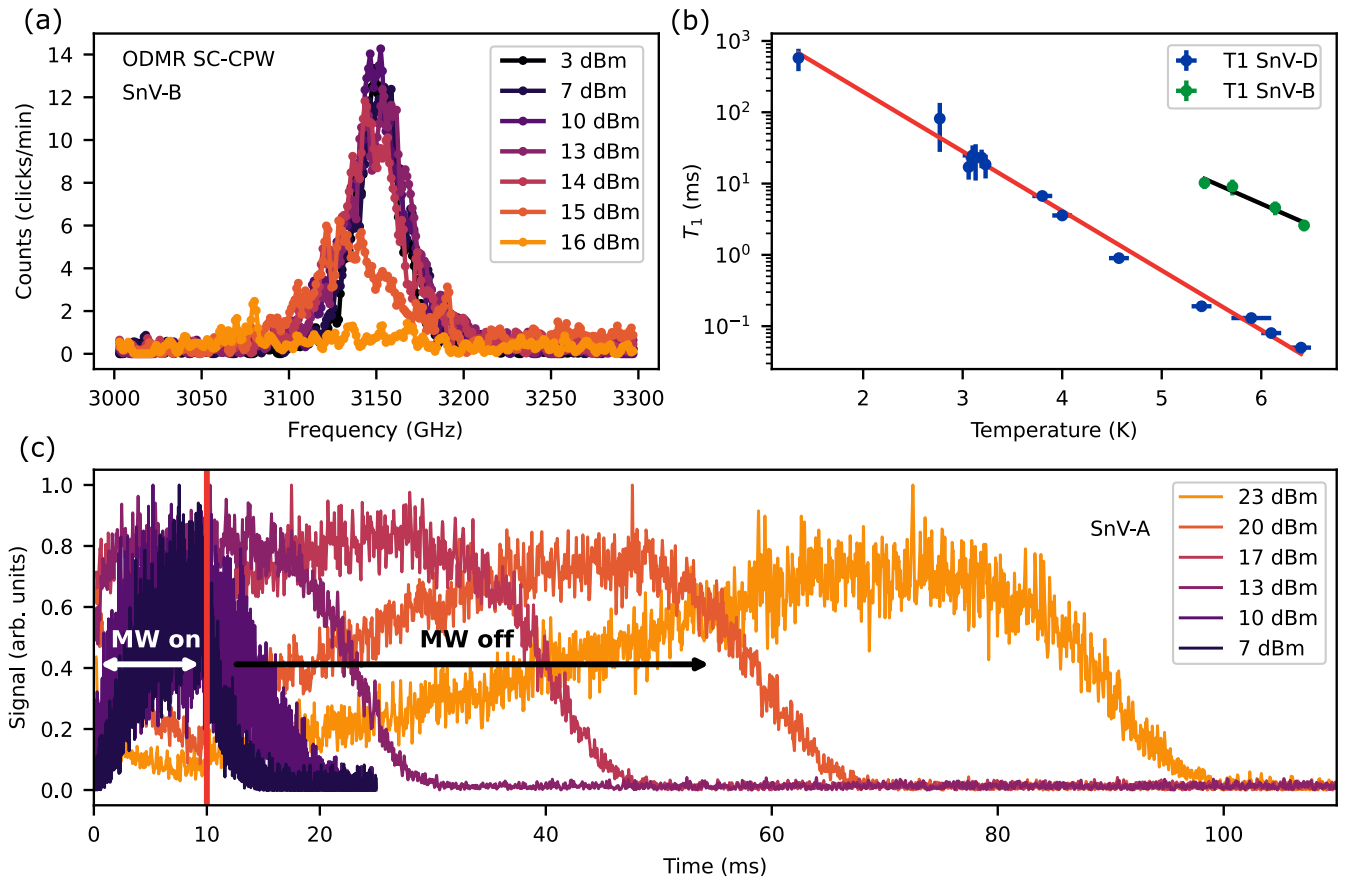


FIG. 8. Heating effect of NC-CPW versus SC-CPW and  $T_1$  for an unstrained and a highly strained SnV center. (a) ODMR measurement of the highly strained SnV-B with SC-CPW. The signal decays above 14 dBm, possibly due to the breaking of superconductivity. The ODMR is measured by applying a repetitive microwave (MW) chirp for 10 ms followed by a 190-ms waiting time. The total measurement duration is 2 min for each ODMR. (b)  $T_1$  measurement on an unstrained (blue points) and a highly strained (green points) SnV center. The strained SnV shows a significantly higher spin lifetime due to the larger ground-state splitting. (c) Heating effect of NC-CPW for off-resonant cw-microwave drive at 3 GHz with a 10-ms duration followed by a 190-ms break. The heightened local temperature causes an increased count rate by thermal repopulation of the continuously pumped readout state. Similar curves were observed in Ref. [12].

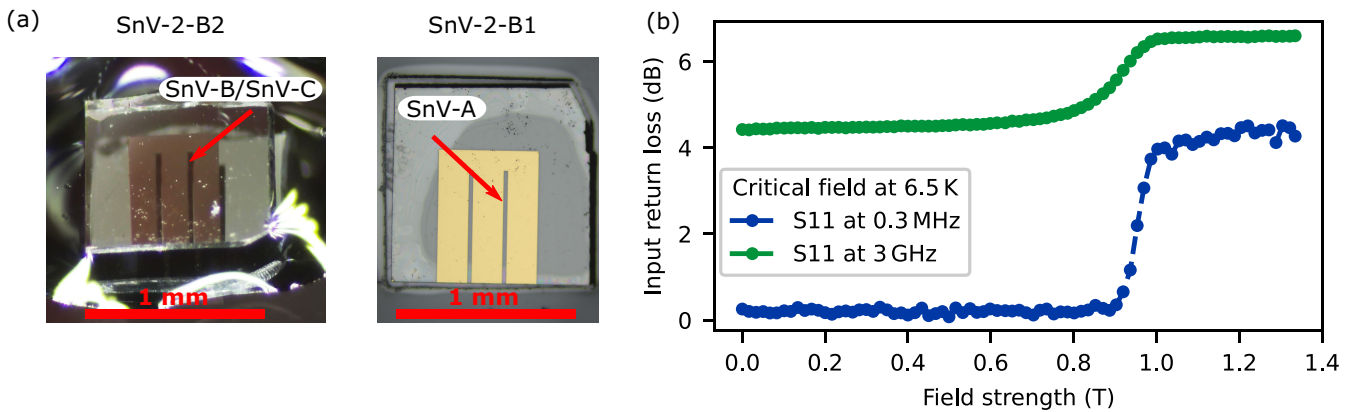


FIG. 9. Images of the SC-CPW and NC-CPW samples, and critical field measurement. (c) Left: SC-CPW sample SnV-2-B2 with the niobium waveguide. Right: NC-CPW sample SnV-2-B1 with the gold waveguide. (d) Critical field measurement of the SC-CPW sample at 6.5 K. The critical field is reached at about 0.95 T, as is visible by the sharp increase of the input return loss S11.

applied magnetic field can be determined. Additionally, in the calibration process, we implement a field modulation technique, oscillating the magnetic field to asymptotically approach and stabilize at the target value. For the spin-echo measurement parallel to the SnV axis ( $z$  component), we fit to a single-frequency coupling, arising from the  $^{13}\text{C}$  spin bath:

$$p_{\parallel}(\tau) = A \exp\left(B \sin^4(2\pi f \tau + \varphi) - \frac{\tau}{T_{\text{damp}}}\right) + a\tau + \text{dc}. \quad (\text{B1})$$

The equation attributes phenomenologically for additional coupling to other carbon-13 spins visible in the echo decay shown in Fig. 10(a) by artificially introducing a damping time and a linear increase. The fit is in good agreement with a Lorentzian fit to the FFT of the echo signal, but it yields a better uncertainty compared to the FFT. For the spin-echo measurement perpendicular to the SnV axis ( $y$  component), shown in Fig. 10(c), we follow the same procedure. Interestingly, the coupling of the proximal nuclear spin is now visible; thus, we use the equation derived in Ref. [41] for NV centers coupled to a proximal  $^{13}\text{C}$  spin as a function:

$$p_{\perp}(\tau) = A \sin(2\pi f_1 \tau)^2 \sin(2\pi f_2 \tau)^2 + \text{dc}. \quad (\text{B2})$$

One frequency corresponds to the spin bath and one to the proximal nuclear spin. As reported in Ref. [41], the precession of the proximal nuclear spin is enhanced; thus, we attribute the higher frequency to it. The expected Larmor precession of the bath is given by

$$\begin{aligned} f_{\text{Larmor}} &= \gamma_{^{13}\text{C}} B \\ &= 10.7084 \text{ MHz T}^{-1} 100 \text{ mT} \\ &= 1.07084 \text{ MHz}. \end{aligned} \quad (\text{B3})$$

The ratio between the measured frequency and the expected one gives the corrected amplitude of the magnetic field,

$$B_{\text{par}} = 96.7(2) \text{ mT}, \quad (\text{B4})$$

$$B_{\text{perp}} = 94.5(4) \text{ mT}. \quad (\text{B5})$$

However, we overestimate the error for the magnetic field coils to be 0.5% to account for effects like hysteresis for the following Hamiltonian fits and estimations of the

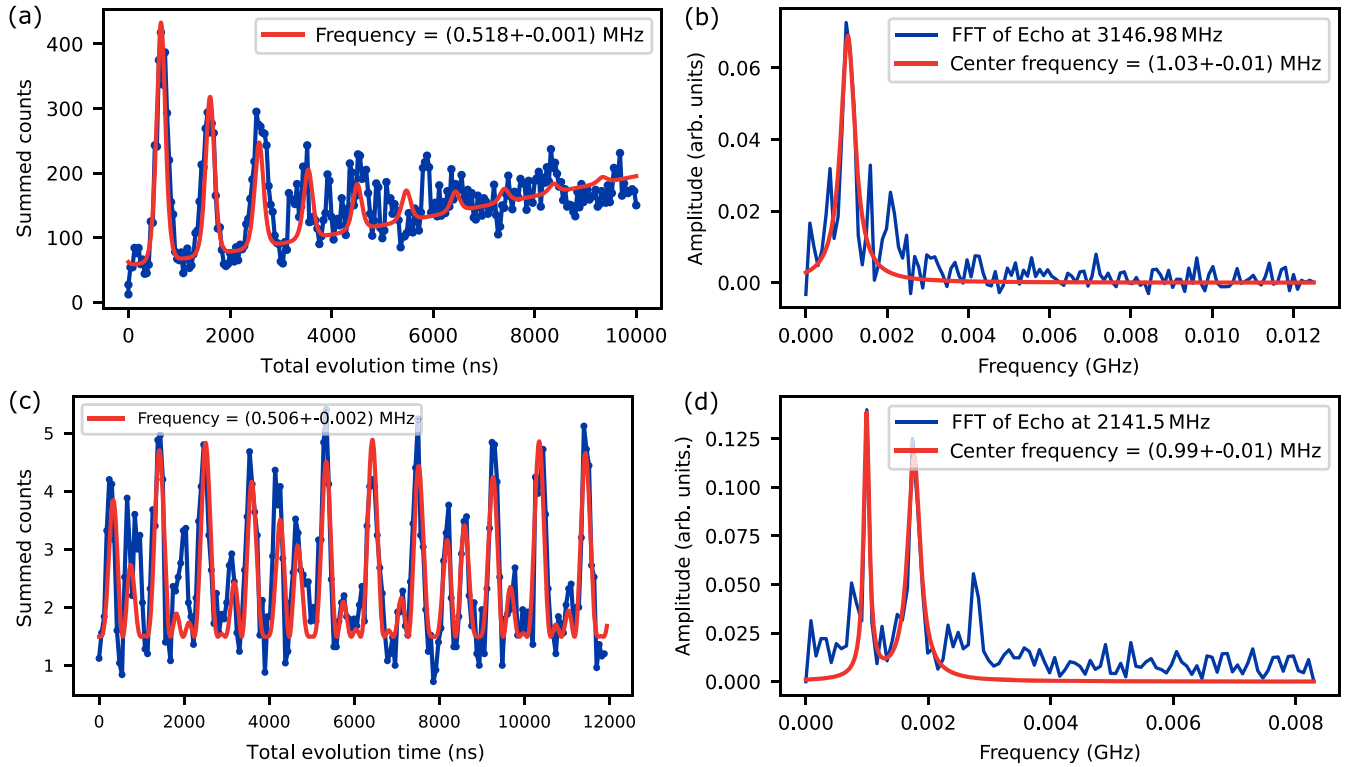


FIG. 10. Hahn-echo signal for parallel (a) and perpendicular (c) orientation of the magnetic field. The echo is modulated by coupling to the  $^{13}\text{C}$  bath. For perpendicular orientation, an additional coupling to a proximal spin is observed, resulting in a beating of the oscillations. The corresponding FFT signal is shown in panels (b) and (d), respectively.

TABLE III. Estimated parameters of magnetic field coils spanning the lab frame and the SnV orientations within this lab frame.

Coil axis	Magnetic field (mT A <sup>-1</sup> )	SnV	Quantization axis (X, Y, Z)
X	-45.7(2)	A	(-0.081, 0.834, -0.546)
Y	61.5(3)	B	(0.011, 0.722, 0.692)
Z	133.5(6)	C	(-0.015, 0.883, -0.468)

orbital quenching factors. For the sake of completeness, we note the current dependency of our 3D-vector magnets in Table III, together with the vectors of the three SnVs (A–C) in the lab frame.

## 2. Derivation of the Hamiltonian

The Hamiltonian of this system is described by four contributions, namely, the spin-orbit coupling, the orbital Zeeman splitting, the spin Zeeman splitting, and the strain splitting, leading to

$$\hat{H}_{\text{eff}}^{\text{g,u}} = -\lambda^{\text{g,u}} \hat{L}_z \hat{S}_z + \mu_B (f_{m_j}^{\text{g,u}})_{\{\pm\frac{1}{2}, \pm\frac{3}{2}\}} \cdot \hat{L}_z B_z + g_S \mu_B \hat{\mathbf{S}} \cdot \mathbf{B} + \hat{\Upsilon}_{\text{strain}} \cdot \quad (\text{B6})$$

The orbital quenching factor is defined as  $f_{m_j}^{\text{g,u}} = g_L^{\text{g,u}} \cdot p_{m_j}^{\text{g,u}}$ , as introduced in Ref. [16], where  $g_L^{\text{g,u}}$  is the Stevens reduction factor for the ground and excited states and  $p_{m_j}$  is the Ham-reduction factor for each effective total-angular-momentum quantum number  $m_j = \{\pm\frac{1}{2}, \pm\frac{3}{2}\}$ . As we are not able to differentiate these two components in our measurements, we focus on the common orbital quenching factor  $f_{m_j}^{\text{g,u}}$ . To derive a matrix representation of the Hamiltonian, for simplicity, we show the derivation for the ground state, which applies equivalently to the excited state. The  $\hat{L}_z$  operator in the  $\{xy\}$  basis of the electronic states, where the  $m_l = 0$  ( $A_{2u}$ ) orbital is far detuned and thus irrelevant [42], is given by the matrix

$$\hat{L}_z = \begin{pmatrix} 0 & i \\ -i & 0 \end{pmatrix}. \quad (\text{B7})$$

The spin-orbit splitting Hamiltonian follows as

$$H_{\text{so}}^{\text{xy}} = -\lambda^{\text{g}} \hat{L}_z \hat{S}_z = \begin{bmatrix} 0 & 0 & -\frac{i\lambda^{\text{g}}}{2} & 0 \\ 0 & 0 & 0 & \frac{i\lambda^{\text{g}}}{2} \\ \frac{i\lambda^{\text{g}}}{2} & 0 & 0 & 0 \\ 0 & -\frac{i\lambda^{\text{g}}}{2} & 0 & 0 \end{bmatrix}, \quad (\text{B8})$$

by performing the outer product between the  $\hat{L}_z$  operator and the  $\sigma_z$  Pauli matrix.

The transformation matrix  $T$ , which diagonalizes  $H_{\text{so}}^{\text{xy}}$  and thus connects the  $\{xy\}$  basis and spin-orbit eigenbasis or short  $\{so\}$  basis, is given by the relation

$$T^{-1} H_{\text{so}}^{\text{xy}} T = H_{\text{so}}^{\text{so}}. \quad (\text{B9})$$

Solving this equation results in the matrix

$$T = \begin{bmatrix} i & 0 & -i & 0 \\ 0 & -i & 0 & i \\ 1 & 0 & 1 & 0 \\ 0 & 1 & 0 & 1 \end{bmatrix}, \quad (\text{B10})$$

and the diagonalized spin-orbit coupling follows as

$$H_{\text{so}}^{\text{so}} = \begin{bmatrix} -\frac{\lambda^{\text{g}}}{2} & 0 & 0 & 0 \\ 0 & -\frac{\lambda^{\text{g}}}{2} & 0 & 0 \\ 0 & 0 & \frac{\lambda^{\text{g}}}{2} & 0 \\ 0 & 0 & 0 & \frac{\lambda^{\text{g}}}{2} \end{bmatrix}. \quad (\text{B11})$$

The spin Zeeman term without any asymmetry contributes to the Hamiltonian as

$$\bar{H}_{\text{Ze}}^{\text{xy}} = \frac{\gamma_s}{2} \begin{bmatrix} B_{\parallel} & B_{\perp} & 0 & 0 \\ B_{\perp} & -B_{\parallel} & 0 & 0 \\ 0 & 0 & B_{\parallel} & B_{\perp} \\ 0 & 0 & B_{\perp} & -B_{\parallel} \end{bmatrix}, \quad (\text{B12})$$

where the parallel magnetic field orientation is chosen along the SnV center quantization axis.

For the orbital Zeeman term, one has to account for the orbital quenching factors  $f_{m_j}$  for each sublevel, with their distinct orbital quantum number  $m_j = \{\pm\frac{1}{2}, \pm\frac{3}{2}\}$ . For the ordering of the substates, we follow Ref. [16], which, in the spin-orbit eigenbasis, leads to the matrix

$$H_{\text{ZL}}^{\text{so}} = \gamma_l B_{\parallel} \begin{bmatrix} f_{32} & 0 & 0 & 0 \\ 0 & -f_{32} & 0 & 0 \\ 0 & 0 & -f_{12} & 0 \\ 0 & 0 & 0 & f_{12} \end{bmatrix}, \quad (\text{B13})$$

where we omitted the fraction in the subscript for better readability. Transforming this matrix into the  $\{xy\}$  basis using the transformation matrix  $T$  results in

$$H_{\text{ZL}}^{\text{xy}} = \frac{\gamma_l B_{\parallel}}{2} \begin{bmatrix} -f_{12} + f_{32} & 0 & if_{12} + if_{32} & 0 \\ 0 & f_{12} - f_{32} & 0 & if_{12} + if_{32} \\ -if_{12} - if_{32} & 0 & -f_{12} + f_{32} & 0 \\ 0 & -if_{12} - if_{32} & 0 & f_{12} - f_{32} \end{bmatrix}. \quad (\text{B14})$$

This result already suggests the emergence of mean values of the reduction factors  $f$  and differences leading to finite asymmetries  $\delta$ , like reported in Ref. [16]. For the full Hamiltonian, we have to account for the strain contribution in the  $\{xy\}$  basis; it is given by

$$H_{\text{JT}}^{\text{xy}} = \begin{bmatrix} \alpha & 0 & 0 & 0 \\ 0 & \alpha & 0 & 0 \\ 0 & 0 & -\alpha & 0 \\ 0 & 0 & 0 & -\alpha \end{bmatrix}, \quad (\text{B15})$$

including strain and Jahn-Teller effects in the coupling constant  $\alpha$  (see, e.g., Ref. [42]). Collecting all of these results, we obtain the full electronic Hamiltonian in the  $\{xy\}$  basis as

$$H_{\text{xy}} = \frac{1}{2} \begin{bmatrix} (\gamma_l(f_{32} - f_{12}) + \gamma_s)B_{\parallel} + 2\alpha & \gamma_s B_{\perp} & i\gamma_l(f_{12} + f_{32})B_{\parallel} - i\lambda^{\text{g}} & 0 \\ \gamma_s B_{\perp} & (\gamma_l(f_{12} - f_{32}) - \gamma_s)B_{\parallel} + 2\alpha & 0 & i\gamma_l(f_{12} + f_{32})B_{\parallel} + i\lambda^{\text{g}} \\ (-i\gamma_l(f_{12} + f_{32}))B_{\parallel} + i\lambda^{\text{g}} & 0 & (\gamma_l(f_{32} - f_{12}) + \gamma_s)B_{\parallel} - 2\alpha & \gamma_s B_{\perp} \\ 0 & -i\gamma_l(f_{12} + f_{32})B_{\parallel} - i\lambda^{\text{g}} & \gamma_s B_{\perp} & (\gamma_l(f_{12} - f_{32}) - \gamma_s)B_{\parallel} - 2\alpha \end{bmatrix}. \quad (\text{B16})$$

The eigenvalues of this matrix are used to fit the measured ODMR data, the difference in the allowed transitions A1 and B2, and if measured, the difference in the forbidden transitions B1 and A2. For the sake of completeness, the Hamiltonian in the  $\{so\}$  basis is given by

$$H_{\text{so}} = \frac{1}{2} \begin{bmatrix} (2f_{32}\gamma_l + \gamma_s)B_{\parallel} - \lambda^{\text{g}} & 0 & -2\alpha & \gamma_s B_{\perp} \\ 0 & (-2f_{32}\gamma_l - \gamma_s)B_{\parallel} - \lambda^{\text{g}} & \gamma_s B_{\perp} & -2\alpha \\ -2\alpha & \gamma_s B_{\perp} & (-2f_{12}\gamma_l + \gamma_s)B_{\parallel} + \lambda^{\text{g}} & 0 \\ \gamma_s B_{\perp} & -2\alpha & 0 & (2f_{12}\gamma_l - \gamma_s)B_{\parallel} + \lambda^{\text{g}} \end{bmatrix}. \quad (\text{B17})$$

We note that we can rewrite this Hamiltonian by introducing the commonly used mean reduction factors  $f = (f_{12}/2) + (f_{32}/2)$ , and the mean asymmetries  $\delta = (f_{32}/2) - (f_{12}/2)$  and  $\gamma_l = (\gamma_s/2)$ , leading to

$$H_{\text{so}} = \begin{bmatrix} (f\gamma_l + \delta\gamma_l + \frac{\gamma_s}{2})B_{\parallel} - \frac{\lambda^{\text{g}}}{2} & 0 & -\alpha & \frac{\gamma_s B_{\perp}}{2} \\ 0 & (-f\gamma_l - \delta\gamma_l - \frac{\gamma_s}{2})B_{\parallel} - \frac{\lambda^{\text{g}}}{2} & \frac{\gamma_s B_{\perp}}{2} & -\alpha \\ -\alpha & \frac{\gamma_s B_{\perp}}{2} & (-f\gamma_l + \delta\gamma_l + \frac{\gamma_s}{2})B_{\parallel} + \frac{\lambda^{\text{g}}}{2} & 0 \\ \frac{\gamma_s B_{\perp}}{2} & -\alpha & 0 & (f\gamma_l - \delta\gamma_l - \frac{\gamma_s}{2})B_{\parallel} + \frac{\lambda^{\text{g}}}{2} \end{bmatrix}. \quad (\text{B18})$$

Accounting for the freedom to rearrange the columns, this matrix is the same Hamiltonian as reported in Ref. [16].

### 3. Fitting procedure and uncertainty estimation

In our procedure, the eigenvalues of the full Hamiltonian are numerically fitted. However, for an intuitive understanding of the different parameters, we analytically calculate the eigenvalues for different strain and magnetic field regimes. First, we look at the qubit transitions for negligible strain  $\alpha^{\text{g}}$ , in comparison to the spin-orbit coupling  $\lambda^{\text{g}}$ . Thus, for parallel orientation of the magnetic field, we have an ODMR splitting of

$$|2\rangle - |1\rangle = B_{\parallel}(2f_{32}^g\gamma_l + \gamma_s), \quad (\text{B19})$$

showing that the qubit transitions at the parallel field only depend on the orbital quenching factor  $f_{32}^g$  in the case of

vanishing strain. Furthermore, under the same conditions, one finds, for the allowed transitions,

$$A1 - B2 = 2B_{\parallel}(f_{32}^g - f_{32}^u)\gamma_l. \quad (\text{B20})$$

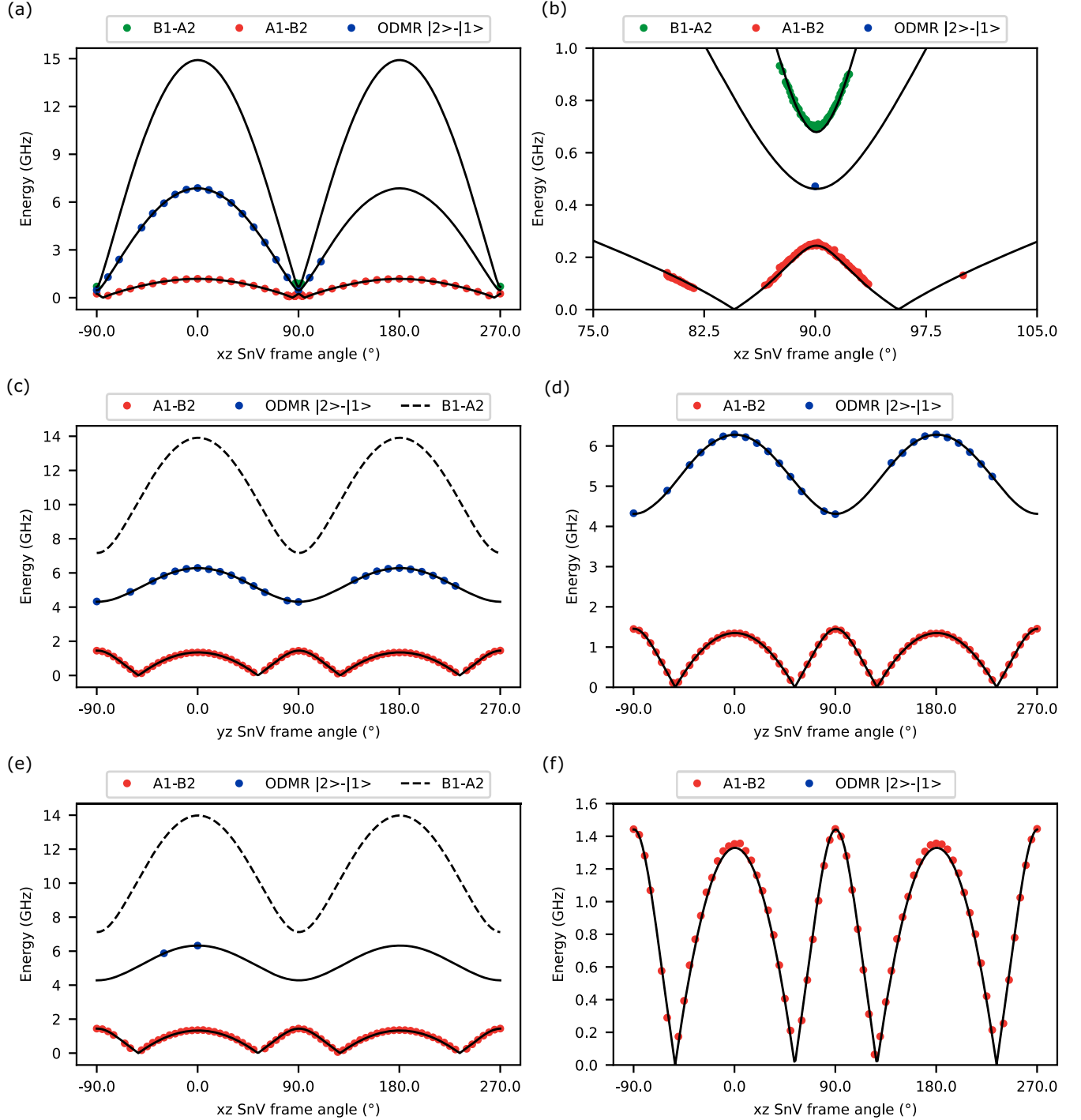


FIG. 11. Fit of the Hamiltonian. (a),(b) Low-strain SnV-A. This emitter is used to determine  $f_{32}^{g,u}$ . Because of the low branching ratio at the perpendicular magnetic field orientation ( $\theta = 90^\circ$ ), the forbidden transitions B1-A2 are detectable (black dots) at temperatures where the spin lifetime is much shorter than the sweeping speed of the PLE measurement. (c),(d) High-strain SnV-B. This emitter is used to determine  $f_{32}^{g,u}$ . (e),(f) High-strain SnV-C. This emitter is used to validate the fitting parameters  $f_{1\frac{3}{2}}^{g,u}$ .

Hence, by using the value of  $f_{32}^g$  that we obtain from fitting the qubit transitions, the excited-state quenching factor  $f_{32}^u$  can be determined by fitting the allowed transitions.

To determine the exact strain magnitude, one can look at the splitting of the qubit at the perpendicular field orientation, which follows as

$$|2\rangle - |1\rangle = \frac{1}{2} \left( \sqrt{(\gamma_s B_\perp - 2\alpha^g)^2 + (\lambda^g)^2} - \sqrt{(\gamma_s B_\perp + 2\alpha^g)^2 + (\lambda^g)^2} \right). \quad (\text{B21})$$

The excited-state strain can be found equivalently via the allowed transitions

$$A1 - B2 = \frac{1}{2} \left( \sqrt{(\gamma_s B_\perp - 2\alpha^u)^2 + (\lambda^u)^2} - \sqrt{(\gamma_s B_\perp + 2\alpha^u)^2 + (\lambda^u)^2} - \sqrt{(\gamma_s B_\perp - 2\alpha^g)^2 + (\lambda^g)^2} + \sqrt{(\gamma_s B_\perp + 2\alpha^g)^2 + (\lambda^g)^2} \right). \quad (\text{B22})$$

For higher strain magnitude, we can determine the quenching factors  $f_{12}^{g,u}$ , as the eigenvalues now also depend on this value. For the qubit transition, we find

$$|2\rangle - |1\rangle = \frac{1}{2} \left( \sqrt{(\lambda^g - \gamma_l B_\parallel (f_{12}^g + f_{32}^g)^2) + 4(\alpha^g)^2} - \sqrt{(\lambda^g + \gamma_l B_\parallel (f_{12}^g + f_{32}^g)^2) + 4(\alpha^g)^2} + 2\gamma_l B_\parallel (f_{12}^g - f_{32}^g) - 2B_\parallel \gamma_s \right), \quad (\text{B23})$$

which allows us to determine  $f_{12}^g$ . With the same approach as before, we can now determine the last quenching factor  $f_{12}^u$  via the allowed transitions. We omit the analytical expression due to the size of the equation.

The resulting fits of the three different investigated SnV centers to the Hamiltonian eigenvalues are shown in Fig. 11. With the estimated error on the magnetic field magnitude of 0.5%, we evaluate the resulting quenching factors with a varying amplitude of  $B_{dc}$  given by

$$B_{dc}^{\parallel,\perp}(x) = B_{\text{mean}}^{\parallel,\perp}(1 + x0.5\%), \quad x \in \{-1, 1\}. \quad (\text{B24})$$

We omit errors on the fit of the allowed transitions, as well as on the ODMR transitions, as these uncertainties are at least an order of magnitude smaller than the obtained values and are negligible compared to the uncertainty stemming from the magnetic field amplitude. As the influence of the error on  $\lambda^g$ , and thus on the strain  $\alpha^g$ , is also small compared to the uncertainty on the magnetic field magnitude, this uncertainty is not propagated onto the quenching parameters either. The result of the fitting procedure is shown in Fig. 12. The range of the obtained quenching parameters is taken as the standard deviation for our estimation.

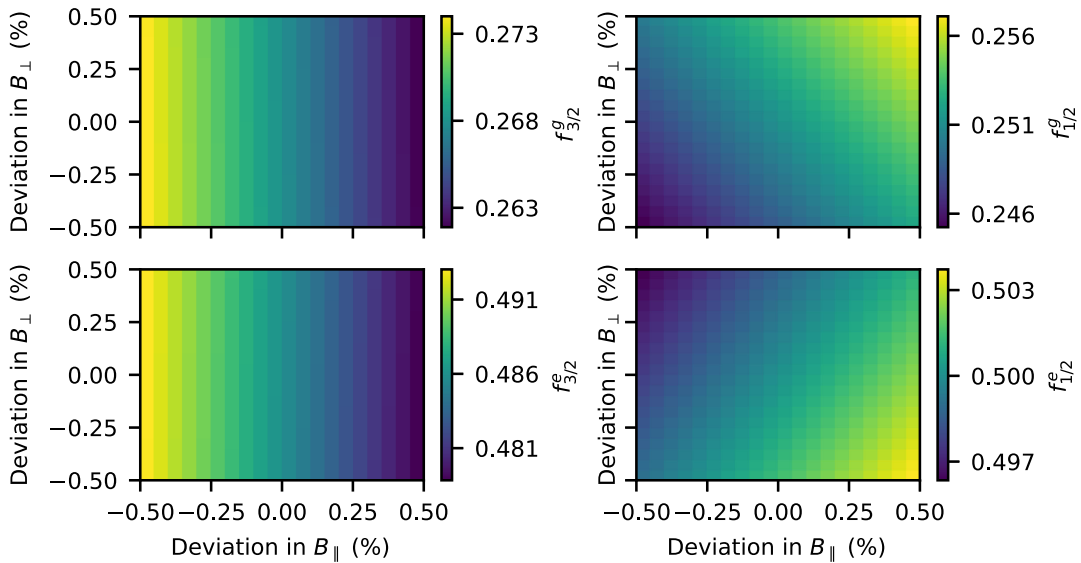


FIG. 12. Spread of the quenching  $f$  parameters from fits to SnV-A and SnV-B, assuming an uncertainty of  $\pm 0.5\%$  on the  $B$ -field amplitude. For each magnetic field strength, the Hamiltonian is fit, and the resulting  $f$  parameter is plotted in the corresponding pixel. As discussed in Appendix B, first  $f_{3/2}^g$  is fitted, followed by  $f_{1/2}^g$ ,  $f_{3/2}^u$ , and  $f_{1/2}^u$ , each taking the previous quenching parameter into account. The total spread of the  $f$  parameters in each subplot is taken as the standard uncertainty for this  $f$  parameter.

#### 4. Optical properties of the SnV center

In Fig. 13(a), we show the lifetime measurement of SnV-B, along with a single PLE scan, demonstrating the excellent optical properties of the SnV center even under the influence of strain. We measure a lifetime of 6.67(48) ns, in accordance with the transform-limited linewidth in Fig. 13(b). The polar plots of the unstrained emitter SnV-D are depicted in Figs. 14(a) and 14(b) in the  $xy$  and  $yz$  lab frames. In contrast to strained SnV centers, the degeneracy of the allowed transitions A1 and B2 is not lifted for the perpendicular field orientation.

#### APPENDIX C: COHERENT CONTROL

We perform the coherence measurements in a parallel magnetic field of 93 mT and apply a resonant microwave with 10 dBm at 3149.1 MHz, resulting in a 196-ns-long  $\pi$

pulse. Reading out and initializing involve a resonant pulse of 1.2 ms to 2.0 ms. After each data point, the charge state is assessed through threshold counting, and a green repump pulse is applied, if necessary. However, no green repump is applied during the dynamical decoupling sequence. We apply a  $+(\pi/2)$  pulse at the end of the decoupling sequence in phase relative to the initial  $+(\pi/2)$  pulse. The recorded data are the cumulative count over the entire readout time. Furthermore, we normalize the data such that the final saturating points (i.e., last ten data points taken) correspond to a fidelity of 0.5 [19]. We fit the normalized data to the function

$$A \exp\left(-\left(\frac{N\tau}{T_2}\right)^\xi\right) + 0.5, \quad (\text{C1})$$

where  $A$  represents the amplitude,  $N$  is the number of decoupling pulses, and  $\xi$  denotes the stretching factor, set at

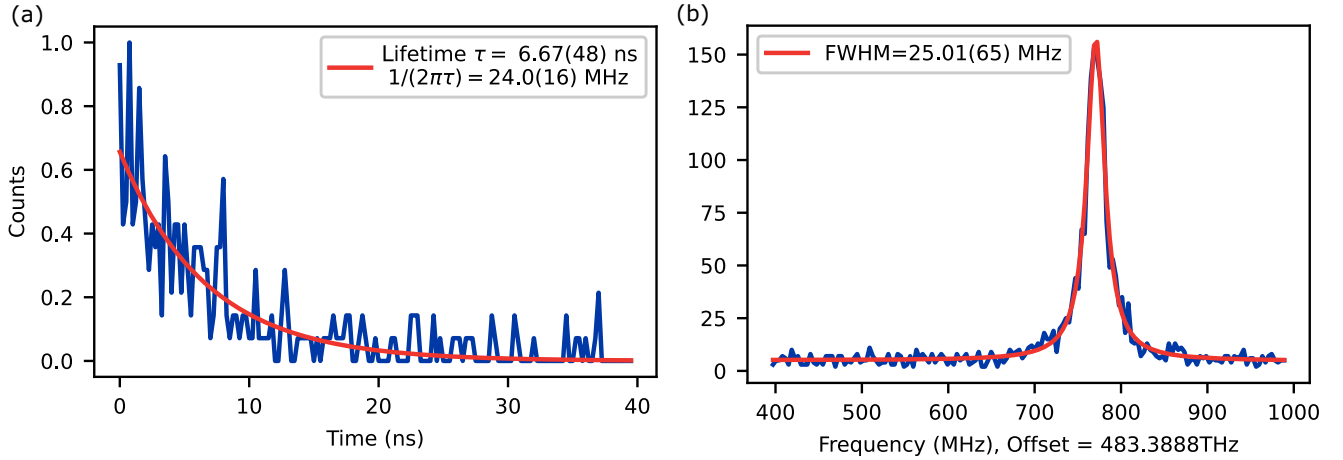


FIG. 13. Single-scan PLE linewidth (left panel) and pulsed resonant lifetime measurement (right panel). The optical linewidth is given by the lifetime and thus is Fourier limited.

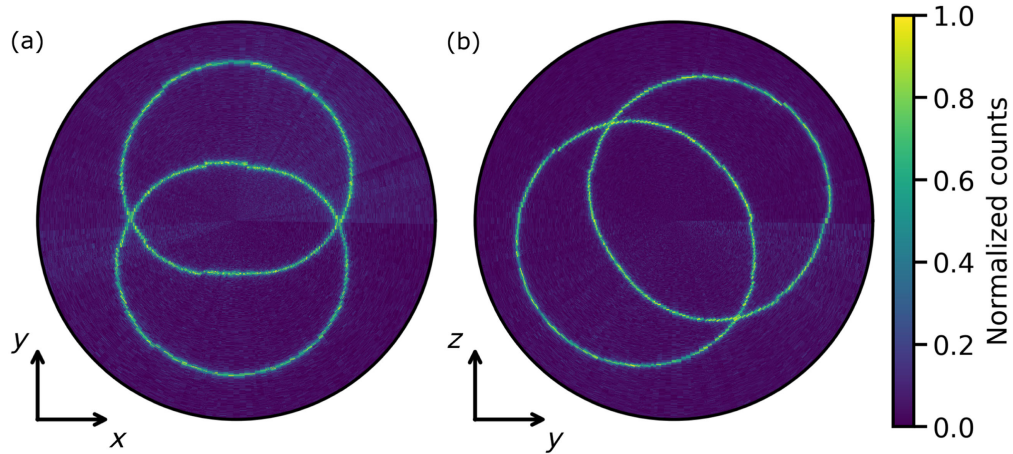


FIG. 14. Polar plots of the unstrained SnV-D in the lab frame. (a) Splitting of the A1 and B2 transitions in the  $xy$  axis of the laboratory frame of SnV-D. The PLE scans are shown in polar coordinates, where the radial axis spans a 1.5-GHz range. (b) Measurement in the  $yz$  axis and a PLE span of 2 GHz. In contrast to strained SnV centers, no splitting is visible for the perpendicular field orientation.

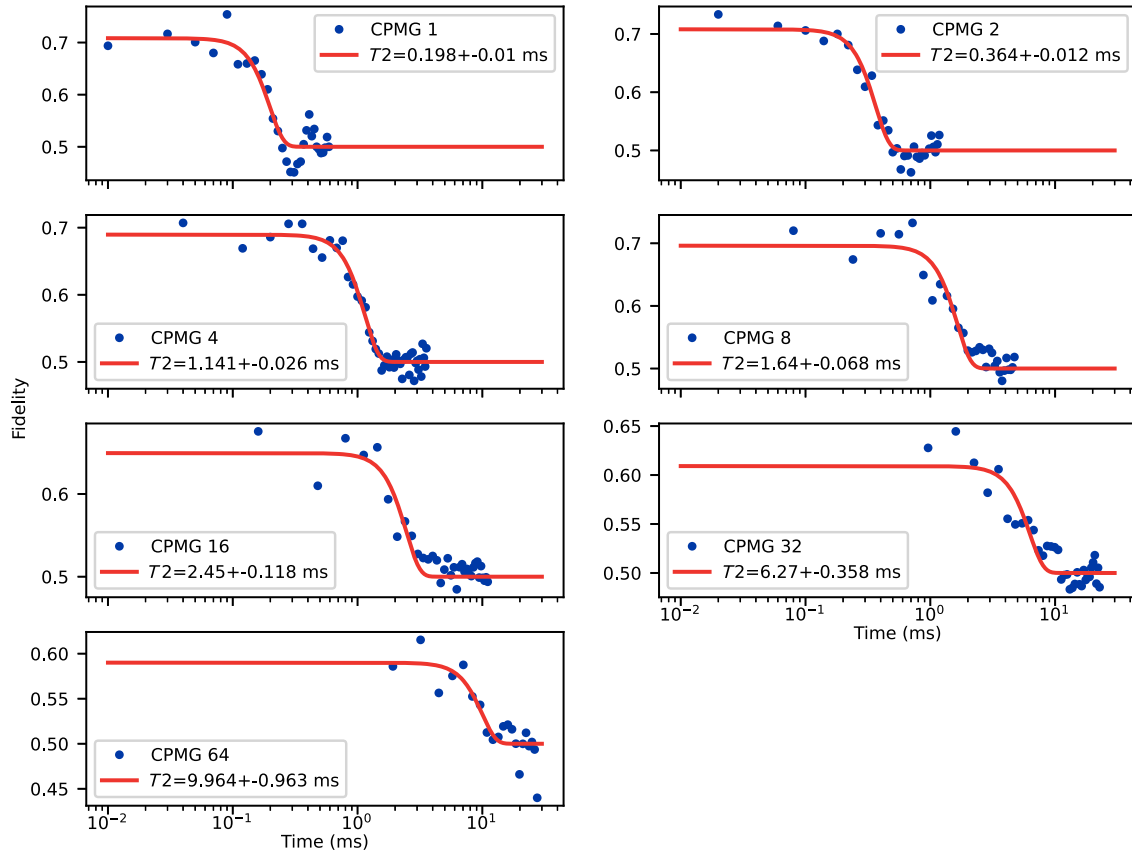


FIG. 15. CPMG sequences with varying number  $N$  of refocusing pulses. The data are scaled to 0.5 for long times and fit to stretched exponential envelopes with  $e^{-(t/T_2)^4}$ .

a constant value of 4 to achieve optimal agreement with the data. The resulting decay curves are shown in Fig. 5. Plotting the obtained coherence times over the number of decoupling pulses, we obtain an exponential increase in  $T_2$ , as shown in Fig. 5.

The observed scaling of the coherence time with the number of  $\pi$  pulses  $n^\beta$  with  $\beta = 1$  deviates from the expected scaling of a single spin bath with  $\beta = \frac{2}{3}$  [34]. To quantify our coherence measurements, we follow the derivation in Ref. [43] by calculating the decoherence function  $W(t) = e^{-\chi(t)}$ , using  $\chi(t)$  in the Gaussian bath approximation as

$$\chi(t) = \int_0^\infty \frac{d\omega}{\pi} \frac{S(\omega)F(\omega t)}{\omega^2}, \quad (\text{C2})$$

with the spectral density of the noise bath  $S(\omega)$  and the filter function  $F(\omega t)$  of the pulse sequence. Using the filter functions

$$F_{\text{Ramsey}}(\omega t) = 2 \sin^2\left(\frac{\omega t}{2}\right), \quad (\text{C3})$$

$$F_{\text{echo}}(\omega t) = 4 \sin^4\left(\frac{\omega t}{4}\right), \quad (\text{C4})$$

$$F_{\text{CPMG}}(\omega t) = 8 \sin^4\left(\frac{\omega t}{4n}\right) \frac{\sin^2\left(\frac{\omega t}{2}\right)}{\cos^2\left(\frac{\omega t}{2n}\right)}, \quad (\text{C5})$$

where  $n$  is the number of pulses, assumed to be an even number [43], one can calculate the effect of different baths on the signal obtained by dynamical decoupling sequences. A bath characterized by Ornstein-Uhlenbeck noise (e.g., P1 centers acting on an NV center diamond [34]) would lead to a Lorentzian spectral density of the noise spectrum,

$$S(\omega) = \frac{b^2}{\pi} \frac{\tau_c}{1 + \omega^2 \tau_c^2}, \quad (\text{C6})$$

with coupling to the local spin  $b$  and the bath correlation time  $\tau_c$  [35,37]. For CPMG sequences, only the high-frequency tail of the Lorentzian is relevant, and it can be described by the power-law scaling  $S(\omega) \propto \omega^{-2}$ . This power-law scaling with  $\omega^{-\alpha}$  leads to decoherence envelopes of

$$W(t) = \exp\left(-\left(\frac{t}{T_2}\right)^\xi\right), \quad (\text{C7})$$

with  $\xi = \alpha + 1$  and scaling  $\beta$ , with the pulse number proportional to the Hahn-echo coherence time

$$T_2^{\text{DD}} = T_2^{\text{HE}} n^\beta, \quad (\text{C8})$$

with  $\beta = (\alpha/\alpha + 1)$  [44]. For an Ornstein-Uhlenbeck bath, this scaling would be  $T_2^{\text{DD}} = T_2^{\text{HE}} \cdot n^{\frac{3}{2}}$ . We find a different scaling of  $T_2^{\text{DD}} = T_2^{\text{HE}} \cdot n^1$  and a different stretched exponential with  $\xi = 4$ . The modeled decoherence function is depicted in Fig. 16(a) and the scaling of the coherence time  $T_2^{\text{DD}}$  is shown in Fig. 16(b). A similar scaling was reported for measurements on the SiV center, observing a second bath in addition to the nuclear spin bath, where a double-Gaussian noise power spectrum,

$$S(\omega) = b_1^2 \exp\left(-\left(\frac{\omega}{\omega_{c1}}\right)^2\right) + b_2^2 \exp\left(-\left(\frac{\omega}{\omega_{c2}}\right)^2\right), \quad (\text{C9})$$

was introduced to describe the observed scaling and stretching of the decoherence function [19]. Using couplings  $b_1^2 = 30 \mu\text{s}^{-1}$ ,  $b_2^2 = 25 \text{ns}^{-1}$  and cutoff frequencies  $\omega_{c1} = 50 \text{s}^{-1}$ ,  $2 \text{ms}^{-1}$ , which are of the same order as the reported coefficients, for a Hahn-echo sequence, we find a stretched exponential with a stretching factor of  $\xi = 4$  and a coherence time  $T_2^{\text{HE}} \approx 170 \mu\text{s}$ , which is in good agreement with the Hahn-echo measurement. In addition, this noise spectrum yields an FID time  $T_2^* \approx 2.5 \mu\text{s}$ , which can be fit to the FID decay. We note that, as mentioned in Sukachev *et al.* [19], a similar result can be obtained by using a double-Lorentzian bath with a hard frequency cutoff. We implement this process by setting the cutoff to  $\omega_{\text{lim}} = 10 \cdot \max(\omega_{c1}, \omega_{c2}) \approx 1 \times 10^4 \text{s}^{-1}$ , using a reasonably fast exponential cutoff of the second spin bath [38]. This method leads to the total bath [37]

$$S(\omega) = \frac{2b_1^2\tau_{c1}}{1 + \omega^2\tau_{c1}^2} + \frac{2b_2^2\tau_{c2}}{1 + \omega^2\tau_{c2}^2} \exp\left(-\left(\frac{\omega}{\omega_{\text{lim}}}\right)^4\right). \quad (\text{C10})$$

We attribute the first bath to the bulk environment of the SnV with a coupling  $b_1$  related to the FID decay time  $b_1 = \frac{\sqrt{2}}{T_2^*} \approx 2\pi \times 100 \text{kHz}$  and the correlation time to the Hahn-echo time for the perpendicular field orientation,

$$\tau_{c1} = \frac{b_1^2}{12} (T_2^{\text{HE}})^3 \approx 3 \text{s}, \quad (\text{C11})$$

as discussed in Ref. [34]. These parameters are in good agreement with reported measurements on the bulk spin bath with deep GeV centers, assuming Ornstein-Uhlenbeck noise [45]. Because of the close proximity to the surface, we add a second surface-charge-induced bath of free electrons [36,37]. Using a coupling  $b_2 = 2\pi \times 30 \text{kHz}$  and correlation time  $\tau_{c2} = 5 \mu\text{s}$ , which are of the same order of magnitude as reported for measurements on shallow NV [37] and SiV centers [36], yields a bath with two quasistatic contributions and a  $\omega^{-2}$  scaling of the bulk spin bath. This double bath reproduces the observed echo time  $T_2^{\text{HE}} \approx 180 \mu\text{s}$  with a stretching factor of  $\xi = 4$  for a Hahn-echo sequence. We find an FID decay of  $T_2^* \approx 2.2 \mu\text{s}$  and a perpendicular (bath one only) echo coherence time  $T_2^{\text{HE}} \approx 440 \mu\text{s}$  with a stretching of  $\xi = 3$ , in good agreement with the measured results and supporting the picture that one can cancel out the electron spin bath by detuning the qubit frequency from the free-electron Larmor precession [15]. In addition, the same scaling of the coherence time with the number of CPMG pulses can be retrieved. Thus, by implementing a hard cutoff in our bath, we can model our measurements by two spin baths, each characterized by an Ornstein-Uhlenbeck process, with a frequency cutoff of  $\omega_{\text{lim}} = 1 \times 10^4 \text{s}^{-1}$ , which is of the same order of magnitude, with reported cutoffs modeling the nuclear spin bath using spin qubits in GaAs [38]. The cutoff frequency of the noise spectrum is given by the fastest possible flip-flop rate of two bath spins [34]; thus,

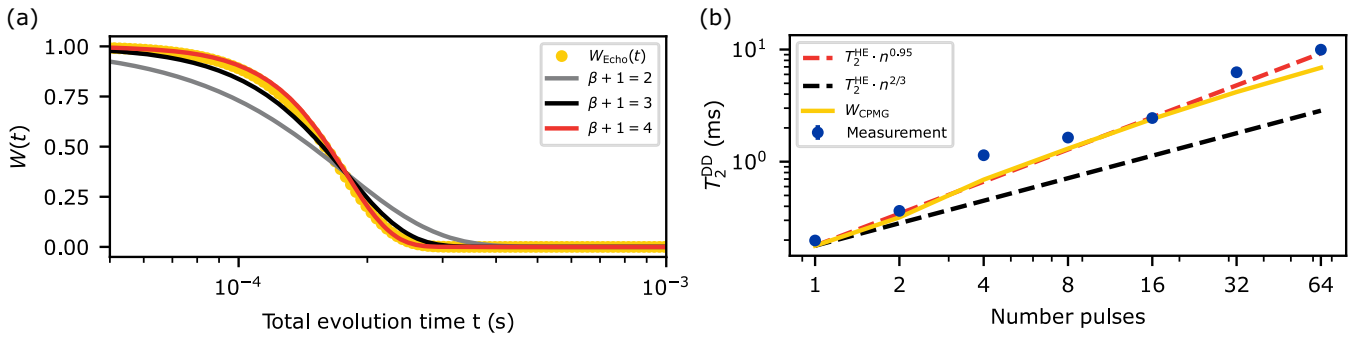


FIG. 16. Properties of a double-Lorentzian bath with a hard cutoff. (a) Modeled decoherence function  $W(t)$ , corresponding to a stretched exponential of power 4, in good agreement with the results shown in Fig. 15. (b) Modeled scaling of the coherence times  $T_2^{\text{DD}}$  with the number of applied  $\pi$  pulses. For  $W_{\text{CPMG}}$ , the  $1/e$  decay is taken as the coherence time  $T_2^{\text{DD}}$ . The data measured are taken from Fig. 5(b).

we attribute the cutoff to intrabath coupling in the electron spin bath [38]. We note that this noise power spectrum, in contrast to the double-Gaussian bath presented in the first part, should result in the single Lorentzian scaling  $n^{2/3}$  for a higher number of pulses, as only the bulk spin bath contributes significantly.

#### APPENDIX D: RABI FREQUENCIES FOR DIFFERENT MAGNETIC FIELD ORIENTATIONS

We observe higher Rabi frequencies for a perpendicular orientation of the magnetic field with respect to the SnV axis. Figures 4(c), 4(d), and 17 show chevron Rabi patterns and Ramsey fringes for parallel and perpendicular orientations of the magnetic field. All patterns are measured using 14-dBm microwave power. Because of the coupling to the proximal nuclear spin, the Rabi frequency for zero detuning depends on the relative splitting of the nuclear spin states. This splitting changes with the orientation of the magnetic field, resulting in a splitting of 4 MHz (5.7 MHz) for a parallel (perpendicular) field orientation. Thus, the detuning-corrected Rabi frequencies can be calculated, resulting in a frequency of 3.6 MHz (5.3 MHz) for a parallel (perpendicular) field orientation. We note that the resonance frequency of the qubit also changes with varying magnetic field angle (see Fig. 2 in the main text), from 3135 MHz to 2150 MHz for parallel and perpendicular orientations, respectively. The transmission losses of the microwave into the cryostat decrease by about 0.5 dB for the roughly 1 GHz lower microwave frequency at perpendicular field orientation compared to the parallel field orientation. The frequency dependent insertion loss into the cryostat can be derived from the measurement in Fig. A7 (a).

#### APPENDIX E: ADHESIVE-INDUCED STRAIN ANALYSIS

To evaluate the strain magnitude induced by the optical adhesive in the diamond, we use the software COMSOL. We assume a diamond thickness of 26  $\mu\text{m}$  and a polymer drop with a diameter of 2 mm and a thickness of 150  $\mu\text{m}$ . The diamond is assumed to be immersed 5  $\mu\text{m}$  deep in the polymer. Since the coefficient of thermal expansion (CTE) for NOA63 is unknown, we use the CTE from a similar adhesive, NOA61 [46]. For simplicity, we approximate the CTE of the adhesive by a steplike function with expansion coefficients  $[230, 90, 80] \times 10^{-6} \text{ K}^{-1}$  changing at temperature steps [270, 230, 4] K and a linear transition range over  $\frac{1}{5}$  of the temperature range between each step. The modulus of elasticity is taken to be constant as 1.6 GPa for the whole temperature range, which is given as a typical value by the manufacturer [47]. The resulting strain components are calculated over the whole diamond surface. The results are shown in Fig. 18. To convert the strain components  $\epsilon'$  into the reference frame of the SnV center, the tensor is rotated according to

$$\epsilon = R_z(\theta)R_y(\phi)\epsilon'R_y(\phi)^\dagger R_z(\theta)^\dagger, \quad (\text{E1})$$

with the angles  $\theta = 90^\circ$  and  $\phi = 54^\circ$ . Because of the different orientations, we find differences in the resulting values for all  $\langle 111 \rangle$  directions. Using the definitions of the strain components with respect to the symmetry,

$$\epsilon_{A_1} = t_\perp(\epsilon_{xx} + \epsilon_{yy}) + t_\parallel\epsilon_{zz}, \quad (\text{E2})$$

$$\epsilon_{E_x} = d(\epsilon_{xx} - \epsilon_{yy}) + f\epsilon_{zx}, \quad (\text{E3})$$

$$\epsilon_{E_y} = -2d\epsilon_{xy} - f\epsilon_{yz}, \quad (\text{E4})$$

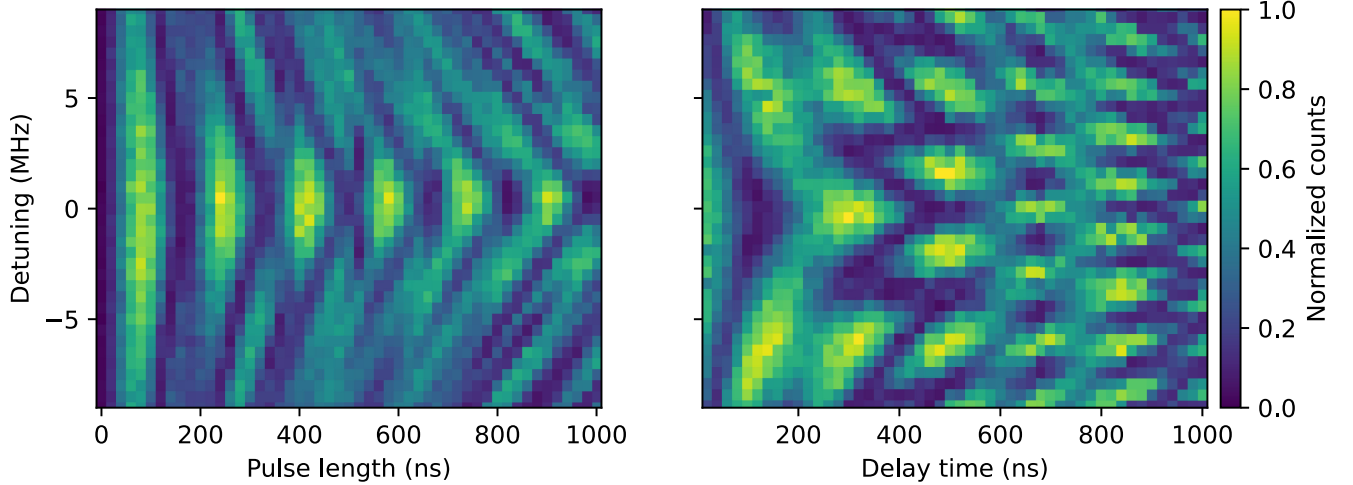


FIG. 17. Left (right) panel: chevron pattern of a Rabi (Ramsey) measurement for 14-dBm driving power and a perpendicular field to the quantization axis (pointing in the  $y$  direction of the SnV orthonormal system) of 100 mT and thus a transition frequency of 2150 MHz.

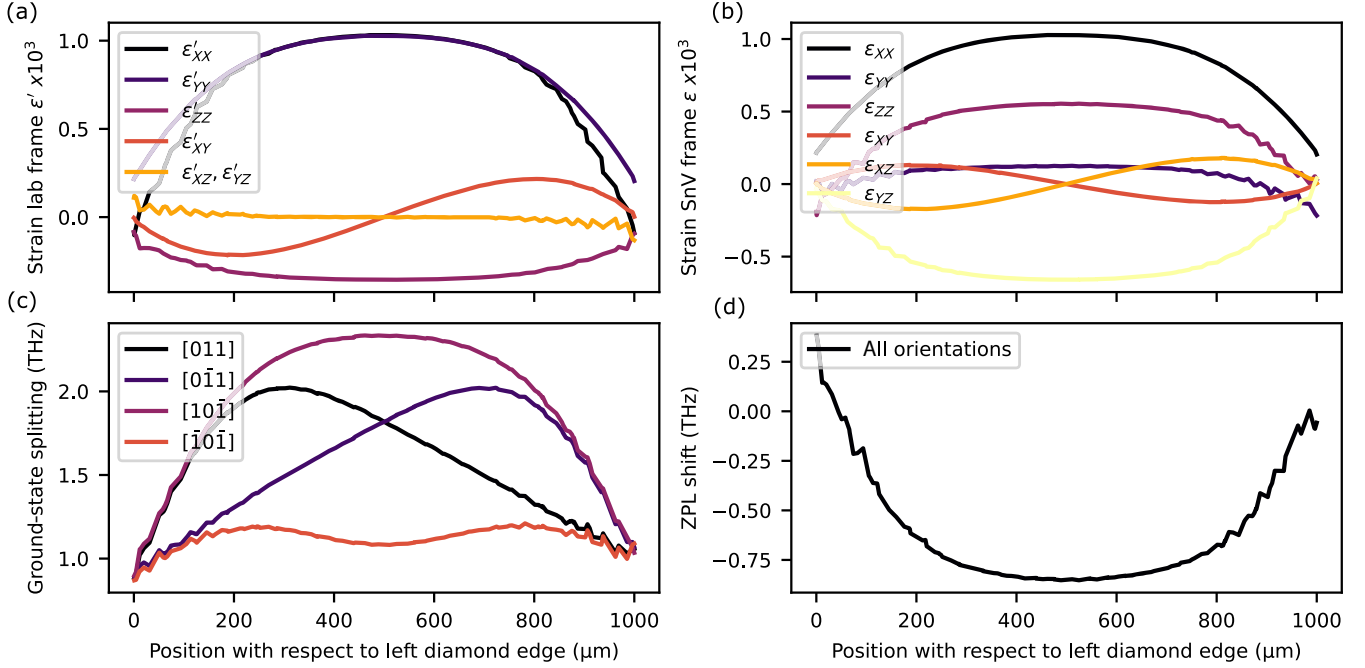


FIG. 18. Strain simulation results. (a) Strain magnitudes for different Cartesian directions in the lab frame. (b) Rotated strain magnitudes with respect to the exemplary possible SnV axis [011]. (c) Calculated ground-state splitting for all four SnV center orientations. We denote the orientations of the SnV center axis within a diamond with  $\langle 110 \rangle$  edges, corresponding to the set  $[111, 1\bar{1}\bar{1}, \bar{1}1\bar{1}, \bar{1}\bar{1}1]$ . (d) Calculated shift of the ZPL as a function of the position of the SnV center along the cut shown in Fig. 1(f). Strain susceptibilities of the SiV (see Ref. [17]) are used to calculate the shift. Because of the symmetry, all orientations observe the same splitting.

and the susceptibilities  $f = -0.56 \times 10^6$  GHz and  $d = 0.8 \times 10^6$  GHz [14], the strain tensor

$$H_{\text{strain}} = \begin{pmatrix} \epsilon_{A1} - \epsilon_{E_x} & \epsilon_{E_y} \\ \epsilon_{E_y} & \epsilon_{A1} + \epsilon_{E_x} \end{pmatrix} \otimes \begin{pmatrix} 1 & 0 \\ 0 & 1 \end{pmatrix} \quad (\text{E5})$$

can be diagonalized. Finally, the corresponding ground-state splittings are calculated by taking the differences of the eigenvalues. To calculate the shift of the ZPL line, we use the

measured values of the SiV,  $t_{\parallel} = -1.7 \times 10^6$  GHz and  $t_{\perp} = 0.078 \times 10^6$  GHz, taken from Ref. [17]. The shift of the ZPL is shown in Fig. 18, and it is in qualitative agreement with the 1-nm shift observed over the half of the diamond shown in Fig. 1. As the simulated ground-state splitting shows a more complex substructure than the measured ground-state splitting, we have to emphasize that this simulation is just a qualitative analysis. Better results can be obtained by using a specified geometry [14] or by simulating with the measured (not assumed) properties of the polymer.

- [1] H. J. Kimble, *The quantum internet*, *Nature (London)* **453**, 1023 (2008).
- [2] M. Atatüre, D. Englund, N. Vamivakas, S.-Y. Lee, and J. Wrachtrup, *Material platforms for spin-based photonic quantum technologies*, *Nat. Rev. Mater.* **3**, 38 (2018).
- [3] E. Togan, Y. Chu, A. S. Trifonov, L. Jiang, J. Maze, L. Childress, M. V. G. Dutt, A. S. Sørensen, P. R. Hemmer, A. S. Zibrov, and M. D. Lukin, *Quantum entanglement between an optical photon and a solid-state spin qubit*, *Nature (London)* **466**, 730 (2010).
- [4] B. Hensen, H. Bernien, A. E. Dréau, A. Reiserer, N. Kalb, M. S. Blok, J. Ruitenber, R. F. L. Vermeulen, R. N. Schouten, C. Abellán, W. Amaya, V. Pruneri, M. W. Mitchell,

- M. Markham, D. J. Twitchen, D. Elkouss, S. Wehner, T. H. Taminiau, and R. Hanson, *Loophole-free Bell inequality violation using electron spins separated by 1.3 kilometres*, *Nature (London)* **526**, 682 (2015).
- [5] H. Bernien, B. Hensen, W. Pfaff, G. Koolstra, M. S. Blok, L. Robledo, T. H. Taminiau, M. Markham, D. J. Twitchen, L. Childress, and R. Hanson, *Heralded entanglement between solid-state qubits separated by three metres*, *Nature (London)* **497**, 86 (2013).
- [6] C. M. Knaut, A. Suleymanzade, Y.-C. Wei, D. R. Assumpcao, P.-J. Stas, Y. Q. Huan, B. Machiels, E. N. Knall, M. Sutula, G. Baranes, N. Sinclair, C. De-Eknamkul, D. S. Levonian, M. K. Bhaskar, H. Park, M. Lončar, and

- M. D. Lukin, *Entanglement of nanophotonic quantum memory nodes in a telecommunication network*, *Nature (London)* **629**, 573 (2024).
- [7] S. L. N. Hermans, M. Pompili, H. K. C. Beukers, S. Baier, J. Borregaard, and R. Hanson, *Qubit teleportation between non-neighbouring nodes in a quantum network*, *Nature (London)* **605**, 663 (2022).
- [8] M. Pompili, S. L. N. Hermans, S. Baier, H. K. C. Beukers, P. C. Humphreys, R. N. Schouten, R. F. L. Vermeulen, M. J. Tiggeleman, L. dos Santos Martins, B. Dirkse, S. Wehner, and R. Hanson, *Realization of a multinode quantum network of remote solid-state qubits*, *Science* **372**, 259 (2021).
- [9] M. K. Bhaskar, R. Riedinger, B. Machielse, D. S. Levonian, C. T. Nguyen, E. N. Knall, H. Park, D. Englund, M. Lončar, D. D. Sukachev, and M. D. Lukin, *Experimental demonstration of memory-enhanced quantum communication*, *Nature (London)* **580**, 60 (2020).
- [10] P.-J. Stas, Y. Q. Huan, B. Machielse, E. N. Knall, A. Suleymanzade, B. Pingault, M. Sutula, S. W. Ding, C. M. Knaut, D. R. Assumpcao, Y.-C. Wei, M. K. Bhaskar, R. Riedinger, D. D. Sukachev, H. Park, M. Lončar, D. S. Levonian, and M. D. Lukin, *Robust multi-qubit quantum network node with integrated error detection*, *Science* **378**, 557 (2022).
- [11] E. Bersin *et al.*, *Telecom networking with a diamond quantum memory*, *PRX Quantum* **5**, 010303 (2024).
- [12] R. Debroux, C. P. Michaels, C. M. Purser, N. Wan, M. E. Trusheim, J. Arjona Martínez, R. A. Parker, A. M. Stramma, K. C. Chen, L. de Santis, E. M. Alexeev, A. C. Ferrari, D. Englund, D. A. Gangloff, and M. Atatüre, *Quantum control of the tin-vacancy spin qubit in diamond*, *Phys. Rev. X* **11**, 041041 (2021).
- [13] J. Görlitz, D. Herrmann, P. Fuchs, T. Iwasaki, T. Taniguchi, D. Rogalla, D. Hardeman, P.-O. Colard, M. Markham, M. Hatano, and C. Becher, *Coherence of a charge stabilised tin-vacancy spin in diamond*, *npj Quantum Inf.* **8**, 45 (2022).
- [14] X. Guo, A. M. Stramma, Z. Li, W. G. Roth, B. Huang, Y. Jin, R. A. Parker, J. Arjona Martínez, N. Shofer, C. P. Michaels, C. P. Purser, M. H. Appel, E. M. Alexeev, T. Liu, A. C. Ferrari, D. D. Awschalom, N. Deegan, B. Pingault, G. Galli, F. J. Heremans, M. Atatüre, and A. A. High, *Microwave-based quantum control and coherence protection of tin-vacancy spin qubits in a strain-tuned diamond-membrane heterostructure*, *Phys. Rev. X* **13**, 041037 (2023).
- [15] E. I. Rosenthal, C. P. Anderson, H. C. Kleidermacher, A. J. Stein, H. Lee, J. Grzesik, G. Scuri, A. E. Rugar, D. Riedel, S. Aghaeimeibodi, G. H. Ahn, K. Van Gasse, and J. Vučković, *Microwave spin control of a tin-vacancy qubit in diamond*, *Phys. Rev. X* **13**, 031022 (2023).
- [16] G. Thiering and A. Gali, *Ab initio magneto-optical spectrum of group-IV vacancy color centers in diamond*, *Phys. Rev. X* **8**, 021063 (2018).
- [17] S. Meesala, Y.-I. Sohn, B. Pingault, L. Shao, H. A. Atikian, J. Holzgrafe, M. Gündoğan, C. Stavrakas, A. Sipahigil, C. Chia, R. Evans, M. J. Burek, M. Zhang, L. Wu, J. L. Pacheco, J. Abraham, E. Bielejec, M. D. Lukin, M. Atatüre, and M. Lončar, *Strain engineering of the silicon-vacancy center in diamond*, *Phys. Rev. B* **97**, 205444 (2018).
- [18] B. Pingault, D.-D. Jarausch, C. Hepp, L. Klintberg, J. N. Becker, M. Markham, C. Becher, and M. Atatüre, *Coherent control of the silicon-vacancy spin in diamond*, *Nat. Commun.* **8**, 15579 (2017).
- [19] D. D. Sukachev, A. Sipahigil, C. T. Nguyen, M. K. Bhaskar, R. E. Evans, F. Jelezko, and M. D. Lukin, *Silicon-vacancy spin qubit in diamond: A quantum memory exceeding 10 ms with single-shot state readout*, *Phys. Rev. Lett.* **119**, 223602 (2017).
- [20] S. Pieplow, M. Belhassen, and T. Schröder, *Efficient microwave spin control of negatively charged group IV color centers in diamond*, *Phys. Rev. B* **109**, 115409 (2023).
- [21] J. Heupel, M. Pallmann, J. Körber, D. Hunger, J. P. Reithmaier, and C. Popov, *Fabrication of high-quality thin single-crystal diamond membranes with low surface roughness*, *Phys. Status Solidi A* **220**, 2200465 (2023).
- [22] P. Fuchs, T. Jung, M. Kieschnick, J. Meijer, and C. Becher, *A cavity-based optical antenna for color centers in diamond*, *APL Photonics* **6**, 086102 (2021).
- [23] C. Hepp, T. Müller, V. Waselowski, J. N. Becker, B. Pingault, H. Sternschulte, D. Steinmüller-Nethl, A. Gali, J. R. Maze, M. Atatüre, and C. Becher, *Electronic structure of the silicon vacancy color center in diamond*, *Phys. Rev. Lett.* **112**, 036405 (2014).
- [24] Y. Narita, P. Wang, K. Ikeda, K. Oba, Y. Miyamoto, T. Taniguchi, S. Onoda, M. Hatano, and T. Iwasaki, *Multiple tin-vacancy centers in diamond with nearly identical photon frequency and linewidth*, *Phys. Rev. Appl.* **19**, 024061 (2023).
- [25] J. Görlitz, D. Herrmann, G. Thiering, P. Fuchs, M. Gandil, T. Iwasaki, T. Taniguchi, M. Kieschnick, J. Meijer, M. Hatano, A. Gali, and C. Becher, *Spectroscopic investigations of negatively charged tin-vacancy centres in diamond*, *New J. Phys.* **22**, 013048 (2020).
- [26] *NIST Standard Reference Database 121, Bohr magneton in Hz/T*, <https://physics.nist.gov/cgi-bin/cuu/Value?mubshhz>.
- [27] *NIST Standard Reference Database 121, Electron gyromagnetic ratio*, <https://physics.nist.gov/cgi-bin/cuu/Value?egammae>.
- [28] A. J. Sigillito, H. Malissa, A. M. Tyryshkin, H. Riemann, N. V. Abrosimov, P. Becker, H.-J. Pohl, M. L. W. Thewalt, K. M. Itoh, J. J. L. Morton, A. A. Houck, D. I. Schuster, and S. A. Lyon, *Fast, low-power manipulation of spin ensembles in superconducting microresonators*, *Appl. Phys. Lett.* **104**, 222407 (2014).
- [29] S. A. Wolf, J. J. Kennedy, and M. Nisenoff, *Properties of superconducting rf sputtered ultrathin films of Nb*, *J. Vac. Sci. Technol.* **13**, 145 (1976).
- [30] R. N. Simons, *Coplanar Waveguide Circuits, Components, and Systems* (John Wiley & Sons, New York, 2004).
- [31] M. H. Metsch, K. Senkalla, B. Tratzmiller, J. Scheuer, M. Kern, J. Achard, A. Tallaire, M. B. Plenio, P. Siyushev, and F. Jelezko, *Initialization and readout of nuclear spins via a negatively charged silicon-vacancy center in diamond*, *Phys. Rev. Lett.* **122**, 190503 (2019).
- [32] R. A. Parker, J. Arjona Martínez, K. C. Chen, A. M. Stramma, I. B. Harris, C. P. Michaels, M. E. Trusheim, M. Hayhurst Appel, C. M. Purser, W. G. Roth, D. Englund, and M. Atatüre, *A diamond nanophotonic interface with an optically accessible deterministic electronuclear spin register*, *Nat. Photonics* **18**, 156 (2024).

- [33] P. London, J. Scheuer, J.-M. Cai, I. Schwarz, A. Retzker, M. B. Plenio, M. Katagiri, T. Teraji, S. Koizumi, J. Isoya, R. Fischer, L. P. McGuinness, B. Naydenov, and F. Jelezko, *Detecting and polarizing nuclear spins with double resonance on a single electron spin*, *Phys. Rev. Lett.* **111**, 067601 (2013).
- [34] Z.-H. Wang, G. de Lange, D. Ristè, R. Hanson, and V. V. Dobrovitski, *Comparison of dynamical decoupling protocols for a nitrogen-vacancy center in diamond*, *Phys. Rev. B* **85**, 155204 (2012).
- [35] N. Bar-Gill, L. M. Pham, C. Belthangady, D. Le Sage, P. Cappellaro, J. R. Maze, M. D. Lukin, A. Yacoby, and R. Walsworth, *Suppression of spin-bath dynamics for improved coherence of multi-spin-qubit systems*, *Nat. Commun.* **3**, 858 (2012).
- [36] C. T. Nguyen, D. D. Sukachev, M. K. Bhaskar, B. Machielse, D. S. Levonian, E. N. Knall, P. Stroganov, C. Chia, M. J. Burek, R. Riedinger, H. Park, M. Lončar, and M. D. Lukin, *An integrated nanophotonic quantum register based on silicon-vacancy spins in diamond*, *Phys. Rev. B* **100**, 165428 (2019).
- [37] B. A. Myers, A. Das, M. C. Dartiailh, K. Ohno, D. D. Awschalom, and A. C. Bleszynski Jayich, *Probing surface noise with depth-calibrated spins in diamond*, *Phys. Rev. Lett.* **113**, 027602 (2014).
- [38] M. J. Biercuk and H. Bluhm, *Phenomenological study of decoherence in solid-state spin qubits due to nuclear spin diffusion*, *Phys. Rev. B* **83**, 235316 (2011).
- [39] P. Rembold, N. Oshnik, M. M. Müller, S. Montangero, T. Calarco, and E. Neu, *Introduction to quantum optimal control for quantum sensing with nitrogen-vacancy centers in diamond*, *AVS Quantum Science* **2**, 024701 (2020).
- [40] G. T. Genov, D. Schraft, N. V. Vitanov, and T. Halfmann, *Arbitrarily accurate pulse sequences for robust dynamical decoupling*, *Phys. Rev. Lett.* **118**, 133202 (2017).
- [41] L. Childress, M. V. G. Dutt, J. M. Taylor, A. S. Zibrov, F. Jelezko, J. Wrachtrup, P. R. Hemmer, and M. D. Lukin, *Coherent dynamics of coupled electron and nuclear spin qubits in diamond*, *Science* **314**, 281 (2006).
- [42] C. Hepp, *Electronic structure of the silicon vacancy color center in diamond* (2014), 10.22028/D291-23020.
- [43] L. Cywiński, R. M. Lutchyn, C. P. Nave, and S. Das Sarma, *How to enhance dephasing time in superconducting qubits*, *Phys. Rev. B* **77**, 174509 (2008).
- [44] J. Medford, L. Cywiński, C. Barthel, C. M. Marcus, M. P. Hanson, and A. C. Gossard, *Scaling of dynamical decoupling for spin qubits*, *Phys. Rev. Lett.* **108**, 086802 (2012).
- [45] K. Senkalla, G. Genov, M. H. Metsch, P. Siyushev, and F. Jelezko, *Germanium vacancy in diamond quantum memory exceeding 20 ms*, *Phys. Rev. Lett.* **132**, 026901 (2024).
- [46] Norland Products, *Norland optical adhesive 61*, <https://www.norlandprod.com/adhesives/noa61pg2.html>.
- [47] Norland Products, *Norland optical adhesive 63*, <https://www.norlandprod.com/adhesives/NOA%2063.html>.